

Impact of crystal symmetries and Weyl nodes on high-harmonic generation in Weyl semimetal TaAs

Xiao Zhang,^{1,2,*} Jeroen van den Brink,^{1,2,†} and Jinbin Li^{3,4,‡}

¹*Institute for Theoretical Solid State Physics, Leibniz IFW Dresden, Helmholtzstrasse 20, 01069 Dresden, Germany*

²*Institute of Theoretical Physics and Würzburg-Dresden Cluster of Excellence ct.qmat, Technische Universität Dresden, 01062 Dresden, Germany*

³*Max-Planck-Institut für Physik komplexer Systeme, Nöthnitzerstrasse 38, 01187 Dresden, Germany*

⁴*School of Nuclear Science and Technology, Lanzhou University, Lanzhou 730000, China*

(Dated: May 28, 2024)

High-harmonic generation (HHG) offers an all-optical approach to discern structural symmetries through its selection rules and probe topological phases with its spectral signatures. Here we develop a universal theoretical framework — the Jones matrix formalism — establishing the fundamental relationship between pulse-crystal shared symmetries and HHG selection rules. Applying this to the Weyl semimetal (WSM) material TaAs, shows that the anomalous harmonics excited by linearly and circularly polarized pulses are governed respectively by the shared twofold and fourfold rotational symmetries of laser pulses and lattice, rather than the topology of Weyl nodes. The common observables of HHG, including intensity, circular dichroism, ellipticity dependence, and carrier-envelope phase dependence, are not found to carry a signature of the Weyl cones. This insight into TaAs can be extended to other WSMs, indicating that HHG is not a particularly effective tool for investigating the topological features of WSMs. However, the Jones matrix formalism lays the groundwork for both HHG probing crystal symmetry and controlling harmonic polarization states.

Introduction. Weyl semimetals (WSMs) feature topologically protected linear band crossings known as Weyl points (WPs) in the momentum space [1–4]. Isolated WPs, with right- or left-handed chirality (or topological charge, $\chi = \pm 1$), act as monopoles for Berry curvature, requiring the material to break either spatial inversion (\mathcal{I}) or time-reversal symmetry (\mathcal{T}) for their emergence [5–8]. These unusual electronic features give rise to appealing nonlinear optical effects, like giant photocurrent effects and second-harmonic generation [9–12]. Recently, the exploration of nonlinear optical effects in WSMs has been extended to the realm of strong field physics such as high-harmonic generation (HHG). Experimentally, both odd and even harmonics have been observed in β -WP₂ crystals [13], a type-II WSM characterized by broken \mathcal{I} . Theoretical studies have shown the emergence of anomalous odd harmonics polarized perpendicular to the incident laser field within \mathcal{T} -breaking WSMs [14–16]. However, the mechanism behind the generation of anomalous odd and even harmonics in WSMs is still under debate.

Research over the past decade suggests that HHG holds promise as a potential tool for probing the crystal symmetries [17–19] and topological properties [20–23] of solid-state materials. Observations across a wide range of materials indicate that the mirror and rotational symmetries of lattices are not only reflected in the anisotropic harmonic emissions [24–27] but also in the HHG selection rules [28–30]. In Chern insulators, the helicity and circular dichroism (CD) of the harmonics serve as indicators for characterizing topological phase transitions [31, 32]. For three dimensional topological insulators (3D TIs), the gapless surface states (Dirac cones) and gapped bulk states can be differentiated by the sensitivity of HHG to

the carrier-envelope phase (CEP) [33] and the HHG ellipticity dependence [34–36]. However, it remains unclear whether the crystal symmetry, the distinctive gapless Weyl cones, and the chiral Berry curvature monopoles can leave unique imprints on the high-harmonic (HH) spectra of WSMs. Moreover, a first-principles investigation of the HHG in WSMs, considering the realistic band structure of materials, has not been reported so far.

In this letter, we address two crucial issues: i) What is the intrinsic connection between anomalous harmonics, HHG selection rules, and crystal symmetries? ii) Can HHG be effectively employed to probe Weyl cones in WSMs? We study HHG in TaAs from first principles due to its type-I Weyl cones, which are close to the Fermi energy, making it conducive for Weyl fermionic excitations in the mid-infrared (MIR) spectral range. By developing the Jones matrix formalism, we provide an analytical expression for HHG selection rules, linking the harmonic orders, polarization states, and crystal symmetries. For the second issue, we explore the possible observables of HHG which may reflect the gapless excitations and chiral topological charges of Weyl cones. We find that the anomalous even harmonics are governed by the crystal symmetries rather than the topology of WPs. The HHG CD does not reflect the chirality of topological charge because the mirror symmetries eliminate the overall chirality of TaAs. The occurrence of anomalous HHG ellipticity dependence and sensitive HHG CEP dependence depends more on the values of laser parameters than on the presence of Weyl cones. Blocking Weyl fermionic excitation by tuning chemical potential, the yield of each harmonic is altered slightly and does not exhibit a consistent trend of change. These results imply that all the

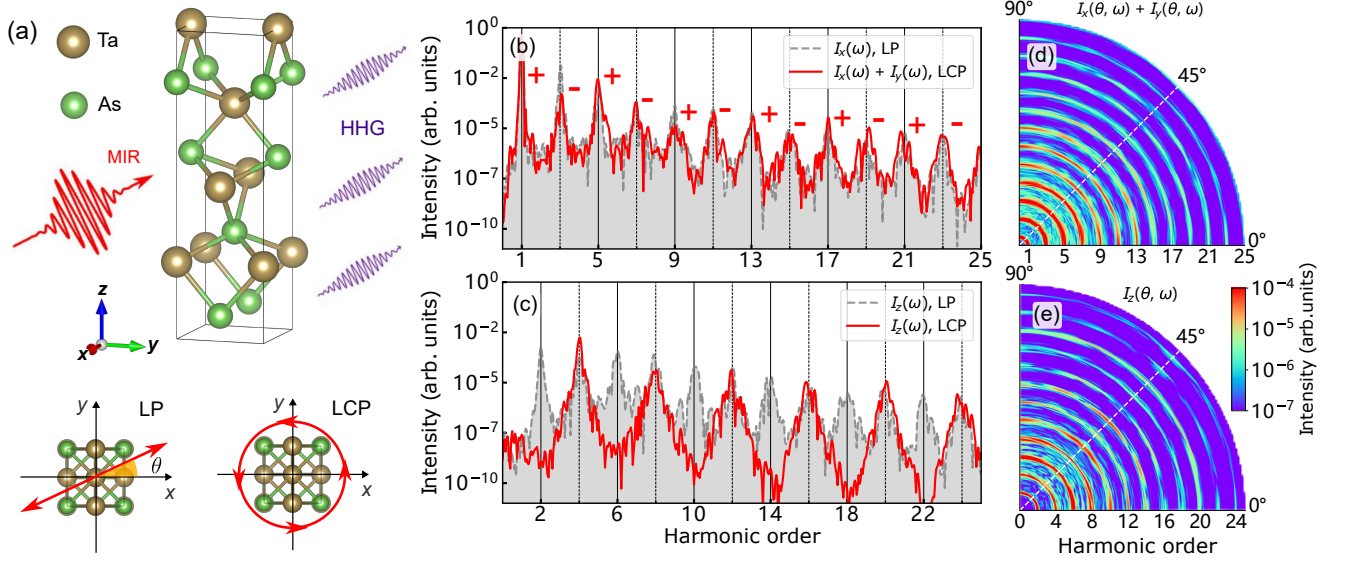


FIG. 1. (a) Sketch of harmonic signals generated by MIR laser interacting with TaAs crystal, where x , y , and z axes are parallel to the $[100]$, $[010]$, and $[001]$ directions, respectively. In inset θ is the angle of LP field relative to the x axis. Harmonic spectra in (b) x - y plane $[(001)$ lattice plane] and (c) z direction obtained by a LP field (gray dashed curves) and by a left-handed circularly polarized driving field (red curves). The plus/minus (+/-) sign indicates harmonic helicity that is the same as/opposite to the helicity of the driving field. Orientation dependence of (d) parallel and (e) transverse harmonics excited by a LP pulse. The laser parameters are intensity $I_0 = 5.04 \times 10^{10}$ W/cm² ($E_0 = 0.0012$ a.u.), wavelength $\lambda = 4200$ nm ($\hbar\omega = 0.295$ eV), and duration $n_{\text{cyc}} = 20$ cycles.

mentioned HHG signatures generally do not probe the topological properties of Weyl semimetals in an efficient manner.

Numerically, we employ a method combining time dependent Schrödinger equation with a first-principles model [37, 38], to calculate HHG in TaAs. Density functional theory (DFT) calculations, for example, band structure and density of states, are performed using Full-Potential Local-Orbital code [39, 40]. The first-principles model is obtained by fitting DFT band structure employing highly localized Wannier functions implemented in PYPFLO module [40]. Details can be found in Supplemental Material (SM) [41]. Atomic units are used throughout this work unless indicated otherwise.

Jones matrix formalism. The studies on the selection rules of solid HHG predominantly rely on experimental induction, numerical simulation, and phenomenological analysis [20, 28, 30], lacking a systematic framework. To fill this void, we develop the Jones matrix method (see the derivation in SM [41]). It shows that the harmonic field $\mathbf{J}(n_H\omega)$ can always be expressed as the product of Jones matrix and Jones vector by taking into account the space group operations in crystals

$$\mathbf{J}(n_H\omega) = \mathcal{J}(n_H) \mathbf{J}^{\text{ir}}(n_H\omega), \quad (1)$$

where n_H is the harmonic order, ω is the laser frequency, and the Jones vector $\mathbf{J}^{\text{ir}}(n_H\omega)$ also represents the irreducible part of the harmonic field. The Jones matrix,

expressed as

$$\mathcal{J}(n_H) = \sum_{l'=1}^{N'} (\mathcal{R}')^{l'} \sum_{l=1}^N \exp(-i2\pi n_H \frac{l}{N}) (\mathcal{R})^l, \quad (2)$$

not only reveals how the crystal symmetry controls the allowed harmonic orders and polarization states but also clarifies the underlying principles of utilizing HHG selection rules to probe crystal symmetry. In Eq. (2), \mathcal{R} and \mathcal{R}' are the shared symmetry matrices of external field and crystal structure, N (N') is the order of symmetry element \mathcal{R} (\mathcal{R}'), i.e., $\mathcal{R}^N = E$ [$(\mathcal{R}')^N = E$]. E is the identity element. Note that \mathcal{R} and \mathcal{R}' are different. The external field, when subjected to the operation of \mathcal{R} , is equivalent to being translated by T/N in time (where T represents the laser cycle), while the external field remains invariant under the operation of \mathcal{R}' .

HHG in TaAs. TaAs is a Weyl semimetal crystallizing in noncentrosymmetric (\mathcal{I} is broken) $I4_1md$ (No.109) structure [42, 43], see Fig. 1(a). It possesses twofold rotation $\mathcal{C}_{2(z)}$, fourfold rotation $\mathcal{C}_{4(z)}$, $\mathcal{C}_{4(-z)}$, and mirror \mathcal{M}_x , \mathcal{M}_y , \mathcal{M}_{xy} , \mathcal{M}_{-xy} symmetries.

We begin by examining harmonic responses in TaAs driven by a linearly polarized (LP) field along the x direction. As shown in Figs. 1(b)-(c) (gray dashed curves), typical odd harmonics are observed in the x (parallel) direction, whereas clear even-structure harmonics manifest in the z (transverse) direction. It is noteworthy that no harmonic response is observed in the y direction. Upon applying a left-handed circularly polarized

(LCP) driver, depicted by the red curves, the circularly polarized odd harmonics emerge with alternating ellipticity (± 1). Along the z direction, the $(4k-2)$ th harmonics disappear while the $(4k)$ th harmonics survive. Moreover, the $(4k)$ th harmonics retain linear polarization.

Parallel harmonics are commonly referred to as ordinary, while transverse harmonics are termed anomalous [44, 45]. The previous studies attribute the generation of anomalous harmonics to the influence of WPs in WSMs [14, 15]. Nonetheless, we think that crystal symmetries are the more fundamental factors resulting in the anomalous harmonics. By using the Jones matrix method [Eq. (2)], all the observations in Figs. 1(b)-(e) can be interpreted. As the LP field is oriented within the x - y plane of TaAs, the shared symmetry \mathcal{R} is $\mathcal{C}_{2(z)}$, see inset of Fig. 1(a). Due to the absence of \mathcal{M}_z (broken \mathcal{I}) in TaAs, there is no additional crystal symmetry that can maintain the LP field invariant when it deviates from the high symmetry axes. Thus, the shared symmetry \mathcal{R}' equals E . Plugging \mathcal{R} and \mathcal{R}' into Eq. (2), the corresponding Jones matrices are expressed as

$$\mathcal{J}(2k+1) = \begin{pmatrix} 1 & & \\ & 1 & \\ & & 0 \end{pmatrix} \quad \mathcal{J}(2k) = \begin{pmatrix} 0 & & \\ & 0 & \\ & & 1 \end{pmatrix}, \quad (3)$$

where $k \in \mathbb{N}$. The $\mathcal{J}(2k+1)$ implies that odd harmonics are allowed in both x and y direction. Nevertheless, $\mathcal{J}(2k)$ serves as a conventional linear polarizer with an axis along z [46], indicating the presence of linearly polarized even harmonics in the z direction. Thereby, the $\mathcal{C}_{2(z)}$ along with the broken \mathcal{M}_z ensures that the purely odd harmonics occur within the x - y plane while the purely even ones appear in the z direction. This explains the orientation-dependent HH spectra in Fig. 1(d)-(e). When the LP pulse is polarized along the x axis (a special case), we have $\mathcal{R} = \mathcal{C}_{2(z)}$ and $\mathcal{R}' = \mathcal{M}_y$. The Jones matrix for even harmonics [$\mathcal{J}(2k)$] remains unchanged, while that for odd harmonics [$\mathcal{J}(2k+1)$] becomes a linear polarizer with an axis along x . This is because \mathcal{M}_y eliminates harmonic emission in the y direction. As a result, odd harmonics manifest only in the x direction while even harmonics still occur in the z direction, as indicated by the gray curves shown in Fig. 1(b)-(c). For the LCP pulse in x - y plane, the shared symmetries are $\mathcal{R} = \mathcal{C}_{4(z)}$ and $\mathcal{R}' = E$. Then the Jones matrices read

$$\mathcal{J}(4k \pm 1) = \begin{pmatrix} \frac{1}{2} & \pm \frac{i}{2} & 0 \\ \mp \frac{i}{2} & \frac{1}{2} & 0 \\ 0 & 0 & 0 \end{pmatrix} \quad \mathcal{J}(4k) = \begin{pmatrix} 0 & & \\ & 0 & \\ & & 1 \end{pmatrix}, \quad (4)$$

where $\mathcal{J}(4k+1)$ is exactly the left circular polarizer, $\mathcal{J}(4k-1)$ represents the right circular polarizer, and $\mathcal{J}(4k)$ is the linear polarizer with z axis [46]. These conform to the selection rule observed from the red curves depicted in Fig. 1(b)-(c). Based on the analysis above,

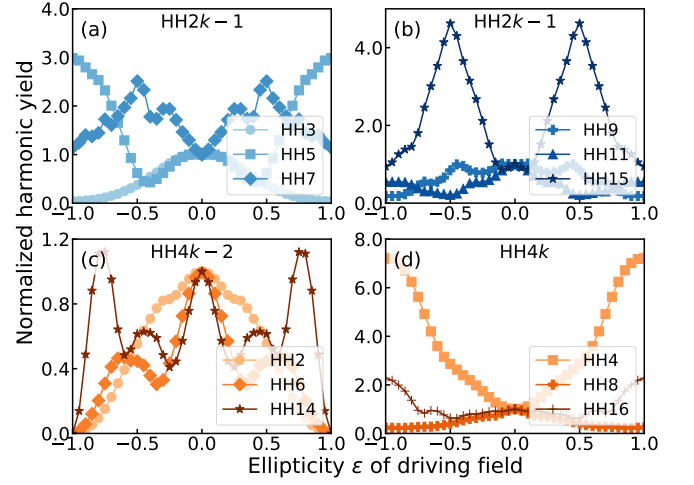


FIG. 2. Normalized yields of $\text{HH}2k-1$ [(a) and (b)], $\text{HH}4k-2$ (c), and $\text{HH}4k$ (d) vs ellipticity of driving field. The laser parameters are the same as those in Fig. 1.

it is reasonable to infer that similar anomalous harmonics can be generated in other materials sharing the same space group as TaAs, for instance, the normal insulator Ba_2S_3 [47].

Impact of Weyl cones on HHG. Next, we shift our focus to the topological properties of TaAs. Circular dichroism, as an approach of assessing chirality, is naturally considered for examining WPs with opposite topological charges. In TaAs, there are 24 WPs in total: 8 WPs situated on the $k_z = 0$ plane, referred to as W_1 , and 16 WPs located away from the $k_z = 0$ plane, referred to as W_2 (see SM [41]). In each subset (W_1 or W_2), WPs are related to each other by $\mathcal{C}_{4(z)}$ and \mathcal{T} . Because of mirror symmetries (\mathcal{M}_x , \mathcal{M}_y , \mathcal{M}_{xy} , and \mathcal{M}_{-xy}), WPs from the same subset are at the same energy even with opposite chirality (χ). The HHG produced by the interaction of a LCP laser with Weyl cone of $\chi = +1$ ($\chi = -1$) are thereby identical to those generated by the interaction of a right-handed circularly polarized (RCP) laser with Weyl cone of $\chi = -1$ ($\chi = +1$). Considering the harmonic contributions across the entire BZ, the HH spectra excited by LCP and RCP pulses are the same. Consequently, the HHG CD in TaAs fails to probe the chirality of WPs, whatever the pulse polarization plane is chosen in the x - y plane, x - z plane, or y - z plane.

In Fig. 2, the yields of a few representative odd and even harmonics are plotted as a function of driver ellipticity. Throughout the ellipticity scan (ranging from -1 to 1), all harmonics exhibit a symmetric profile, with the major axis of the ellipse fixed along the x axis. Specifically, most of the odd harmonics (excluding the 3rd order) in Figs. 2(a)-(b) show an anomalous ellipticity dependence (AED), where the yields of the harmonics are maximized for finite ellipticity. The even harmonics, however, present two distinctly different tendencies.

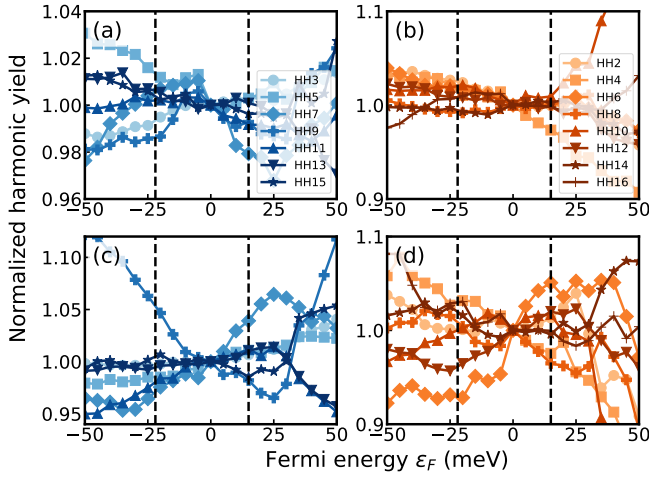


FIG. 3. Normalized harmonic yields as a function of Fermi energy excited by linearly polarized fields with different wavelengths. The blue and orange curves represent odd and even harmonics, respectively. (a) and (b) The laser parameters are $\lambda = 4200$ nm ($\hbar\omega = 0.295$ eV), $I_0 = 5.04 \times 10^{10}$ W/cm² ($E_0 = 0.0012$ a.u.), and $n_{\text{cyc}} = 20$. (c) and (d) The laser parameters are $\lambda = 8400$ nm ($\hbar\omega = 0.148$ eV), $I_0 = 1.26 \times 10^{10}$ W/cm² ($E_0 = 0.0006$ a.u.), and $n_{\text{cyc}} = 20$. The black dashed lines indicate the energies of two nonequivalent sets of WPs (W_1 and W_2) in TaAs.

In Fig. 2(c), the $(4k - 2)$ th harmonics inevitably decay to zero under circular polarization, due to the selection rule constraints. In contrast, the majority of $(4k)$ th (excluding the 8th order) harmonics are enhanced with increasing ellipticity, illustrated in Fig. 2(d). While the 8th harmonic is suppressed under circular polarization, a complete decay is not observed.

In graphene [48, 49] and on the surface of 3D TIs [34, 35], the AED of HHG is attributed to the presence of gapless Dirac cones. However, in TaAs, we cannot establish such a causal relationship between the AED and the presence of Weyl cones. i) HHG ellipticity dependence is highly sensitive to the laser parameters. Employing a pulse with lower intensity and shorter wavelength, we observed significant changes in the ellipticity dependence of HHG, with more harmonics exhibiting normal ellipticity dependence (see SM [41]). ii) In graphene, tuning the chemical potential suppresses the excitation near Dirac cones, leading to a transition from AED to normal ellipticity dependence [49]. However, in TaAs, we employ the same approach to suppress the electron excitation near the Weyl cones. The ellipticity dependence of HHG remains anomalous (see SM [41]). This shows that the Weyl cones do not dominate the HHG ellipticity dependence in TaAs. iii) Furthermore, AED is extensively observed in solid-state systems, including insulators [27, 50], semiconductors [51], and semimetals [48, 49, 52]. Therefore, it cannot serve as a fingerprint for identifying WSMs.

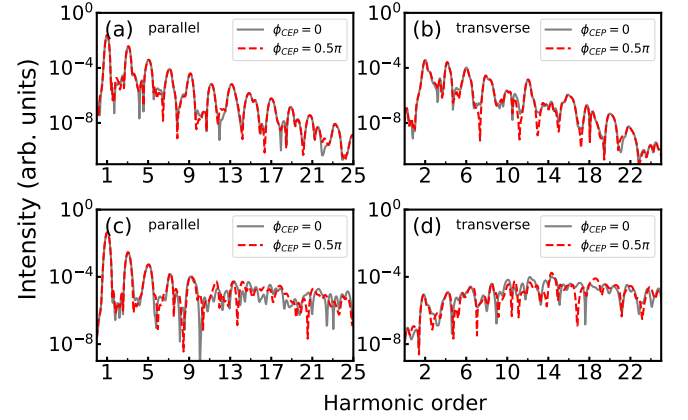


FIG. 4. Parallel and transverse HH spectra excited by few-cycle ($n_{\text{cyc}} = 6$) pulses with different wavelengths. (a) and (b) Wavelength $\lambda = 3200$ nm ($\hbar\omega = 0.388$ eV), and $I_0 = 8.96 \times 10^{10}$ W/cm² ($E_0 = 0.0016$ a.u.). (c) and (d) Wavelength $\lambda = 8400$ nm ($\hbar\omega = 0.148$ eV), and $I_0 = 4.24 \times 10^{10}$ W/cm² ($E_0 = 0.0011$ a.u.). The gray dashed curves and red dashed curves correspond to $\phi_{\text{CEP}} = 0$ and $\phi_{\text{CEP}} = 0.5\pi$, respectively.

In addition to AED, the sensitivity of HHG intensity to excitations of Weyl fermions has been proposed as a possible way to differentiate Weyl cones with different topological charges [16]. Weyl semimetals feature the large tunability of the Fermi level [53, 54]. This provides a feasible experimental approach to block Weyl fermion excitations near the WPs by tuning the chemical potential. In TaAs, the W_1 points are about 15 meV above the Fermi energy ($\varepsilon_F = 0$), while the W_2 points reside about 22 meV below the Fermi level. Figure 3 displays the normalized harmonic yields $[I(n\omega, \varepsilon_F)/I(n\omega, \varepsilon_F = 0)]$ of both ordinary and anomalous harmonics as a function of Fermi energy, ranging from -50 to 50 meV. We do not observe any obvious enhancement or reduction in the harmonic yields, as the Fermi level scans across the energy of the WPs (black dashed lines). The yields of different orders fluctuate within a range of only $\pm 10\%$, for laser pulses with wavelengths of 4200 nm [Figs. 3(a)-(b)] and 8400 nm [Figs. 3(c)-(d)]. At $\varepsilon_F = 50$ meV, there is no visible shift in the energy cutoff of the HH spectra (not show), although all WPs are Pauli blocked. These imply that the intensity of HHG cannot be used to characterize the gapless excitations of electrons near the Weyl cones in TaAs.

Moreover, the dependence of HHG on CEP is also insufficient for discerning the presence of Weyl points. This is because the HH spectra exhibits different sensitivities to the variation of CEP, when the TaAs driven by laser fields with different wavelengths. In Fig. 4(a), the HHG, excited by a LP laser with $\lambda = 3200$ nm, is not sensitive to the CEP. However, a sensitive HHG CEP dependence occurs with increasing the wavelength to $\lambda = 8400$ nm, as shown in Fig. 4(b). This transition in CEP dependence extensively exists in HHG from solids and is not

exclusive to the HHG from WSMs. We attribute it to the change of the harmonic generation from multiphoton ionization-dominated to tunneling ionization-dominated [55].

Conclusion and outlook. In conclusion, we developed the Jones matrix formalism, providing a universal expression for HHG selection rules in crystalline solids. When applied to TaAs, we found that its anomalous even harmonics are induced by the $C_{2(z)}$ symmetry, under the premise of breaking the \mathcal{M}_z (or \mathcal{I}). It is noteworthy that non-topological materials with the same space group can also generate similar anomalous even harmonics. Hence, the anomalous HHG is not a reliable indicator of WSMs. Furthermore, we probed WPs in TaAs by using HHG CD, HHG ellipticity dependence, chemical potential-dependent HHG, and HHG CEP sensitivity. Our observations suggest that these common observables are more influenced by crystal symmetries and laser parameters rather than by the topologically protected Weyl cones. These indicate a similar challenge in detecting WSM topological features with HHG as with probing features of quantum spin/anomalous Hall insulators [56].

These findings for extracting topological features in TaAs can be extended into other semimetal materials, including the other type-I WSMs, type-II WSMs, and Dirac semimetals. In other words, it is impractical to investigate the electronic features of topological semimetals depending solely on harmonic signals induced by monochromatic fields at this stage. The multidimensional optical manipulation may also be a promising method of extracting topology of semimetals. For instance, two-color and multicolor laser fields might be able to maximize the contribution of the electron-hole recombination events highly influenced by the Weyl cones on HHG. In chiral Weyl semimetals (lacking mirror symmetry), the chirality of WP is expected to be measured using HHG CD or HHG elliptical dichroism [12, 57, 58]. It is interesting to observe that even in nonchiral Weyl semimetals, such as TaAs, the chiral anomaly can be induced by applying appropriate external electromagnetic field [59–61], thus breaking mirror symmetries.

Acknowledgements. X.Z. thanks Ulrike Nitzsche for technical assistance. This work is supported by the German Research Foundation (Deutsche Forschungsgemeinschaft, DFG) via SFB1143 Project No. A5 and under Germany's Excellence Strategy through Würzburg-Dresden Cluster of Excellence on Complexity and Topology in Quantum Matter - *ct.qmat* (EXC 2147, Project No. 390858490)

* x.zhang@ifw-dresden.de

† j.van.den.brink@ifw-dresden.de

‡ jinbin@pks.mpg.de

- [1] Gerrit E W Bauer and Laurens W Molenkamp, “Focus on spintronics in reduced dimensions,” *New J. Phys.* **9**, E06 (2007).
- [2] Xiangang Wan, Ari M. Turner, Ashvin Vishwanath, and Sergey Y. Savrasov, “Topological semimetal and Fermi-arc surface states in the electronic structure of pyrochlore iridates,” *Phys. Rev. B* **83**, 205101 (2011).
- [3] A. A. Burkov, M. D. Hook, and Leon Balents, “Topological nodal semimetals,” *Phys. Rev. B* **84**, 235126 (2011).
- [4] Binghai Yan and Claudia Felser, “Topological materials: Weyl semimetals,” *Annu. Rev. Condens. Matter Phys.* **8**, 337–354 (2017).
- [5] Di Xiao, Ming-Che Chang, and Qian Niu, “Berry phase effects on electronic properties,” *Rev. Mod. Phys.* **82**, 1959–2007 (2010).
- [6] Naoto Nagaosa, Jairo Sinova, Shigeki Onoda, A. H. MacDonald, and N. P. Ong, “Anomalous hall effect,” *Rev. Mod. Phys.* **82**, 1539–1592 (2010).
- [7] Andrei Bernevig, Hongming Weng, Zhong Fang, and Xi Dai, “Recent progress in the study of topological semimetals,” *J. Phys. Soc. Jpn.* **87**, 041001 (2018).
- [8] K. Koepernik, D. Kasinathan, D. V. Efremov, Seunghyun Khim, Sergey Borisenko, Bernd Büchner, and Jeroen van den Brink, “TaIrTe₄: A ternary type-II Weyl semimetal,” *Phys. Rev. B* **93**, 201101(R) (2016).
- [9] Liang Wu, S. Patankar, T. Morimoto, N. L. Nair, E. The-walt, A. Little, J. G. Analytis, J. E. Moore, and J. Orenstein, “Giant anisotropic nonlinear optical response in transition metal monpnictide Weyl semimetals,” *Nat. Phys.* **13**, 350–355 (2017).
- [10] O. Matsyshyn and I. Sodemann, “Nonlinear Hall acceleration and the quantum rectification sum rule,” *Phys. Rev. Lett.* **123**, 246602 (2019).
- [11] Zhi Li, Ya-Qin Jin, Takami Tohyama, Toshiaki Iitaka, Jiu-Xing Zhang, and Haibin Su, “Second harmonic generation in the Weyl semimetal TaAs from a quantum kinetic equation,” *Phys. Rev. B* **97**, 085201 (2018).
- [12] Fernando de Juan, Adolfo G. Grushin, Takahiro Morimoto, and Joel E. Moore, “Quantized circular photogalvanic effect in Weyl semimetals,” *Nat. Commun.* **8**, 15995 (2017).
- [13] Yang-Yang Lv, Jinlong Xu, Shuang Han, Chi Zhang, Yadong Han, Jian Zhou, Shu-Hua Yao, Xiao-Ping Liu, Ming-Hui Lu, Hongming Weng, Zhenda Xie, Y. B. Chen, Jianbo Hu, Yan-Feng Chen, and Shining Zhu, “High-harmonic generation in Weyl semimetal β -WP₂ crystals,” *Nat. Commun.* **12**, 6437 (2021).
- [14] Amar Bharti, M. S. Mrudul, and Gopal Dixit, “High-harmonic spectroscopy of light-driven nonlinear anisotropic anomalous Hall effect in a Weyl semimetal,” *Phys. Rev. B* **105**, 155140 (2022).
- [15] H. K. Avetissian, V. N. Avetisyan, B. R. Avchyan, and G. F. Mkrtchian, “High-order harmonic generation in three-dimensional Weyl semimetals with broken time-reversal symmetry,” *Phys. Rev. A* **106**, 033107 (2022).
- [16] Amar Bharti and Gopal Dixit, “Role of topological charges in the nonlinear optical response from Weyl semimetals,” *Phys. Rev. B* **107**, 224308 (2023).
- [17] F. Langer, M. Hohenleutner, U. Huttner, S. W. Koch, M. Kira, and R. Huber, “Symmetry-controlled temporal structure of high-harmonic carrier fields from a bulk crystal,” *Nat. Photonics* **11**, 227–231 (2017).
- [18] Tran Trung Luu and Hans Jakob Wörner, “Measurement of the berry curvature of solids using high-harmonic spec-

- troscopy,” *Nat. Commun.* **9**, 916 (2018).
- [19] Lei Jia, Zhiya Zhang, D. Z. Yang, Yanqing Liu, M. S. Si, G. P. Zhang, and Y. S. Liu, “Optical high-order harmonic generation as a structural characterization tool,” *Phys. Rev. B* **101**, 144304 (2020).
- [20] Ayelet J. Uzan-Narovlansky, Gal Orenstein, Sergei Shames, Matan Even Tzur, Omer Kneller, Barry D. Bruner, Talya Arusi-Parpar, Oren Cohen, and Nirit Dudovich, “Revealing the interplay between strong field selection rules and crystal symmetries,” *Phys. Rev. Lett.* **131**, 223802 (2023).
- [21] Dieter Bauer and Kenneth K. Hansen, “High-harmonic generation in solids with and without topological edge states,” *Phys. Rev. Lett.* **120**, 177401 (2018).
- [22] Christian Heide, Yuki Kobayashi, Denitsa R. Baykusheva, Deepti Jain, Jonathan A. Sobota, Makoto Hashimoto, Patrick S. Kirchmann, Seongshik Oh, Tony F. Heinz, David A. Reis, and Shambhu Ghimire, “Probing topological phase transitions using high-harmonic generation,” *Nat. Photonics* **16**, 620–624 (2022).
- [23] Chen Qian, Chao Yu, Shicheng Jiang, Tan Zhang, Jiacheng Gao, Shang Shi, Hanqi Pi, Hongming Weng, and Ruifeng Lu, “Role of shift vector in high-harmonic generation from noncentrosymmetric topological insulators under strong laser fields,” *Phys. Rev. X* **12**, 021030 (2022).
- [24] Yong Sing You, David A. Reis, and Shambhu Ghimire, “Anisotropic high-harmonic generation in bulk crystals,” *Nat. Phys.* **13**, 345 (2016).
- [25] Hanzhe Liu, Yilei Li, Yong Sing You, Shambhu Ghimire, Tony F. Heinz, and David A. Reis, “High-harmonic generation from an atomically thin semiconductor,” *Nat. Phys.* **13**, 262 (2016).
- [26] Nicolas Tancogne-Dejean, Oliver D. Mücke, Franz X. Kärtner, and Angel Rubio, “Impact of the electronic band structure in high-harmonic generation spectra of solids,” *Phys. Rev. Lett.* **118**, 087403 (2017).
- [27] Nicolas Tancogne-Dejean, Oliver D. Mücke, Franz X. Kärtner, and Angel Rubio, “Ellipticity dependence of high-harmonic generation in solids originating from coupled intraband and interband dynamics,” *Nat. Commun.* **8**, 745 (2017).
- [28] N. Klemke, N. Tancogne-Dejean, G. M. Rossi, Y. Yang, F. Scheiba, R. E. Mainz, G. Di Sciacca, A. Rubio, F. X. Kärtner, and O. D. Mücke, “Polarization-state-resolved high-harmonic spectroscopy of solids,” *Nat. Commun.* **10**, 1319 (2019).
- [29] Óscar Zurrón-Cifuentes, Roberto Boyero-García, Carlos Hernández-García, Antonio Picón, and Luis Plaja, “Optical anisotropy of non-perturbative high-order harmonic generation in gapless graphene,” *Opt. Express* **27**, 7776–7786 (2019).
- [30] Nariyuki Saito, Peiyu Xia, Faming Lu, Teruto Kanai, Jiro Itatani, and Nobuhisa Ishii, “Observation of selection rules for circularly polarized fields in high-harmonic generation from a crystalline solid,” *Optica* **4**, 1333–1336 (2017).
- [31] R. E. F. Silva, Á. Jiménez-Galén, B. Amorim, O. Smirnova, and M. Ivanov, “Topological strong-field physics on sub-laser-cycle timescale,” *Nat. Photonics* **13**, 849–854 (2019).
- [32] Alexis Chacón, Dasol Kim, Wei Zhu, Shane P. Kelly, Alexandre Dauphin, Emilio Pisanty, Andrew S. Maxwell, Antonio Picón, Marcelo F. Ciappina, Dong Eon Kim, Christopher Ticknor, Avadh Saxena, and Maciej Lewenstein, “Circular dichroism in higher-order harmonic generation: Heralding topological phases and transitions in chern insulators,” *Phys. Rev. B* **102**, 134115 (2020).
- [33] C. P. Schmid, L. Weigl, P. Grössing, V. Junk, C. Gorini, S. Schlauderer, S. Ito, M. Meierhofer, N. Hofmann, D. Afanasiev, J. Crewse, K. A. Kokh, O. E. Tereshchenko, J. Gädde, F. Evers, J. Wilhelm, K. Richter, U. Höfer, and R. Huber, “Tunable non-integer high-harmonic generation in a topological insulator,” *Nature (London)* **593**, 385–390 (2021).
- [34] Denitsa Baykusheva, Alexis Chacón, Dasol Kim, Dong Eon Kim, David A. Reis, and Shambhu Ghimire, “Strong-field physics in three-dimensional topological insulators,” *Phys. Rev. A* **103**, 023101 (2021).
- [35] Denitsa Baykusheva, Alexis Chacón, Jian Lu, Trevor P. Bailey, Jonathan A. Sobota, Hadas Soifer, Patrick S. Kirchmann, Costel Rotundu, Ctirad Uher, Tony F. Heinz, David A. Reis, and Shambhu Ghimire, “All-optical probe of three-dimensional topological insulators based on high-harmonic generation by circularly polarized laser fields,” *Nano Lett.* **21**, 8970–8978 (2021).
- [36] Ya Bai, Fucong Fei, Shuo Wang, Na Li, Xiaolu Li, Fengqi Song, Ruxin Li, Zhizhan Xu, and Peng Liu, “High-harmonic generation from topological surface states,” *Nat. Phys.* **17**, 311–315 (2021).
- [37] Yupeng Zhang, Mingying Zhang, Wenli Yang, Haiyuan Yu, M. S. Si, Shan Xue, and Hongchuan Du, “Defects of the nearest-neighbor tight-binding model in the study of solid harmonics,” *Phys. Rev. A* **108**, 043508 (2023).
- [38] R. E. F. Silva, F. Martín, and M. Ivanov, “High harmonic generation in crystals using maximally localized wannier functions,” *Phys. Rev. B* **100**, 195201 (2019).
- [39] Klaus Koepernik and Helmut Eschrig, “Full-potential nonorthogonal local-orbital minimum-basis band-structure scheme,” *Phys. Rev. B* **59**, 1743–1757 (1999).
- [40] <https://www.fplo.de>.
- [41] See Supplemental Material, which includes Refs.[8–10, 36–39].
- [42] L. X. Yang, Z. K. Liu, Y. Sun, H. Peng, H. F. Yang, T. Zhang, B. Zhou, Y. Zhang, Y. F. Guo, M. Rahn, D. Prabhakaran, Z. Hussain, S.-K. Mo, C. Felser, B. Yan, and Y. L. Chen, “Weyl semimetal phase in the non-centrosymmetric compound TaAs,” *Nat. Phys.* **11**, 728–732 (2015).
- [43] Shin-Ming Huang, Su-Yang Xu, Ilya Belopolski, Chih-Cheng Lee, Guoqing Chang, BaoKai Wang, Nasser Alidoust, Guang Bian, Madhab Neupane, Chenglong Zhang, Shuang Jia, Arun Bansil, Hsin Lin, and M. Zahid Hasan, “A Weyl Fermion semimetal with surface fermi arcs in the transition metal monpnictide TaAs class,” *Nat. Commun.* **6**, 7373 (2015).
- [44] Lun Yue and Mette B. Gaarde, “Imperfect recollisions in high-harmonic generation in solids,” *Phys. Rev. Lett.* **124**, 153204 (2020).
- [45] Lun Yue and Mette B. Gaarde, “Characterizing anomalous high-harmonic generation in solids,” *Phys. Rev. Lett.* **130**, 166903 (2023).
- [46] Grant Fowles, *Introduction to Modern Optics*, 2nd ed. (Dover, 1989).
- [47] S. Yamaoka, J. T. Lemley, J. M. Jenks, and H. Stein-fink, “Structural chemistry of the polysulfides dibarium

- trisulfide and monobarium trisulfide,” *Inorg. Chem.* **14**, 129–131 (1975).
- [48] Naotaka Yoshikawa, Tomohiro Tamaya, and Koichiro Tanaka, “High-harmonic generation in graphene enhanced by elliptically polarized light excitation,” *Science* **356**, 736–738 (2017).
- [49] Yongkang Feng, Shaoxi Shi, Jinbin Li, Yajuan Ren, Xiao Zhang, Jianhong Chen, and Hongchuan Du, “Semiclassical analysis of ellipticity dependence of harmonic yield in graphene,” *Phys. Rev. A* **104**, 043525 (2021).
- [50] Yong Sing You, David A. Reis, and Shambhu Ghimire, “Anisotropic high-harmonic generation in bulk crystals,” *Nat. Phys.* **13**, 345–349 (2017).
- [51] Xiao Zhang, Jinbin Li, Zongsheng Zhou, Shengjun Yue, Hongchuan Du, Libin Fu, and Hong-Gang Luo, “Ellipticity dependence transition induced by dynamical bloch oscillations,” *Phys. Rev. B* **99**, 014304 (2019).
- [52] Candong Liu, Yinghui Zheng, Zhinan Zeng, and Ruxin Li, “Driving-laser ellipticity dependence of high-order harmonic generation in graphene,” *Phys. Rev. A* **97**, 063412 (2018).
- [53] O. V. Kotov and Yu. E. Lozovik, “Giant tunable nonreciprocity of light in Weyl semimetals,” *Phys. Rev. B* **98**, 195446 (2018).
- [54] Cheng Guo, Viktor S. Asadchy, Bo Zhao, and Shanhui Fan, “Light control with weyl semimetals,” *eLight* **3**, 2 (2023).
- [55] Huiqiao Wang, Yongkang Feng, Silin Fu, Jinbin Li, Xiao Zhang, and Hongchuan Du, “Complex carrier-envelope-phase effect of solid harmonics under nonadiabatic conditions,” *Phys. Rev. A* **99**, 023406 (2019).
- [56] Ofer Neufeld, Nicolas Tancogne-Dejean, Hannes Hübener, Umberto De Giovannini, and Angel Rubio, “Are there universal signatures of topological phases in high-harmonic generation? Probably not,” *Phys. Rev. X* **13**, 031011 (2023).
- [57] Amar Bharti, Misha Ivanov, and Gopal Dixit, “How massless are Weyl fermions in Weyl semimetals,” *Phys. Rev. B* **108**, L020305 (2023).
- [58] Dylan Rees, Kaustuv Manna, Baozhu Lu, Takahiro Morimoto, Horst Borrmann, Claudia Felser, J. E. Moore, Darius H. Torchinsky, and J. Orenstein, “Helicity-dependent photocurrents in the chiral Weyl semimetal RhSi,” *Sci. Adv.* **6**, eaba0509 (2020).
- [59] Qiong Ma, Su-Yang Xu, Ching-Kit Chan, Cheng-Long Zhang, Guoqing Chang, Yuxuan Lin, Weiwei Xie, Tomás Palacios, Hsin Lin, Shuang Jia, Patrick A. Lee, Pablo Jarillo-Herrero, and Nuh Gedik, “Direct optical detection of Weyl fermion chirality in a topological semimetal,” *Nat. Phys.* **13**, 842–847 (2017).
- [60] Chao-Xing Liu, Peng Ye, and Xiao-Liang Qi, “Chiral gauge field and axial anomaly in a Weyl semimetal,” *Phys. Rev. B* **87**, 235306 (2013).
- [61] A. A. Zyuzin and A. A. Burkov, “Topological response in Weyl semimetals and the chiral anomaly,” *Phys. Rev. B* **86**, 115133 (2012).

Supplementary Material: Impact of crystal symmetries and Weyl nodes on high-harmonic generation in Weyl semimetal TaAs

Xiao Zhang,^{1,2} Jeroen van den Brink,^{1,2} and Jinbin Li^{3,4}

¹*Institute for Theoretical Solid State Physics, Leibniz IFW Dresden, Helmholtzstrasse 20, 01069 Dresden, Germany*

²*Institute of Theoretical Physics and Würzburg-Dresden Cluster of Excellence ct.qmat, Technische Universität Dresden, 01062 Dresden, Germany*

³*Max-Planck-Institut für Physik komplexer Systeme, Nöthnitzerstrasse 38, 01187 Dresden, Germany*

⁴*School of Nuclear Science and Technology, Lanzhou University, Lanzhou 730000, China*

In Supplementary I, we show the methods for Density functional theory (DFT), Wannier projection, and high-harmonic generation (HHG) calculation. Supplementary II illustrates HHG in TaAs with and without spin-orbit coupling (SOC). Supplementary III shows the derivation and application of Jones matrix formalism. In Supplementary IV, we discuss the impact of inversion symmetry breaking on HHG by using a four-band minimal model of TaAs. Supplementary V shows orientation dependence of HHG in TaAs. In supplementary VI, we calculate the circular dichroism of HHG in TaAs with different polarization planes. Supplementary VII exhibits ellipticity dependence of HHG, where the laser parameters and Fermi levels are different from those in the main text.

I. METHODS

A. DFT calculation, Wannier fit, and Weyl point searching

The DFT calculations are carried out for TaAs using the Full-Potential Local-Orbital code (FPLO) code [1], version 21.61. [2] The Perdew-Burke-Ernzerhof implementation of the generalized gradient approximation is employed in our calculations. For the numerical integration of DFT calculations, we use a k mesh with $(12 \times 12 \times 12)$ intervals in the Brillouin zone (BZ). The linear tetrahedron method is used for the numerical integration in the BZ. As applicable, the full relativistic correction is used, while the spin-orbit coupling effects are included via the 4-spinor formalism as implemented in the FPLO code.

TaAs belongs to the space group $I4_1md$ (No.109) with lattice constants $a = b = 3.4348 \text{ \AA}$ and $c = 11.641 \text{ \AA}$.

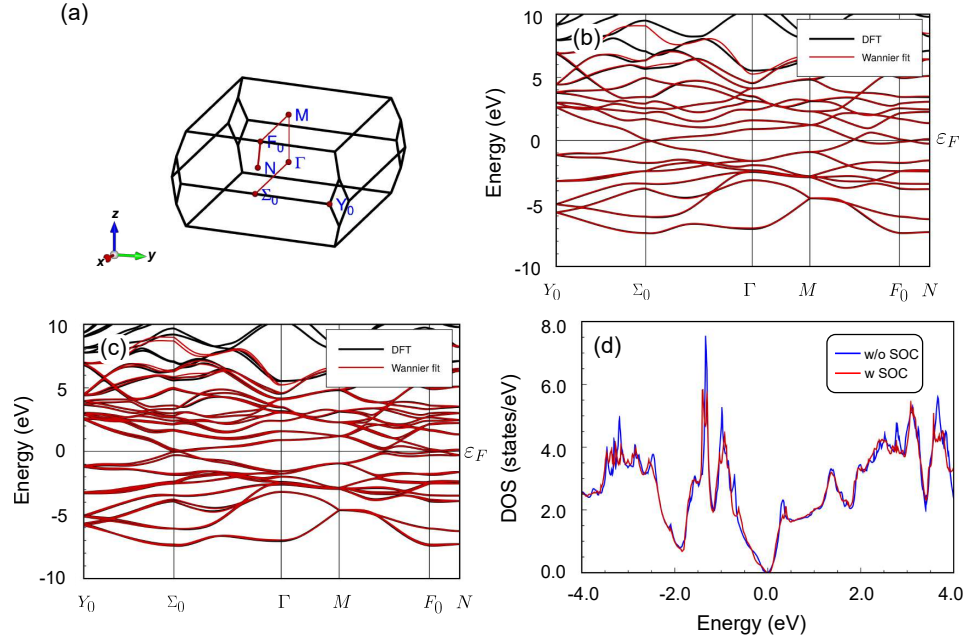


FIG. S1. (a) Sketch of TaAs Brillouin zone with high symmetry paths. (b) Band structure of TaAs without SOC by DFT (black curves) and Wannier fit (red curves). (c) Same as panel (b) but with SOC. (d) DOSs of TaAs without (blue curve) and with SOC (red curve).

TABLE S1. The two nonequivalent Weyl points of TaAs. Positions, Chirality (χ), and energies. Only the coordinates and Chirality of WPs in the first quadrant are given, the others can be obtained through symmetries.

	(k_x, k_y, k_z) in $\frac{2\pi}{a}$	χ	E (meV)
W_1	(0.048, 0.515, 0.000)	+1	15
W_2	(0.031, 0.236, 0.172)	-1	-22

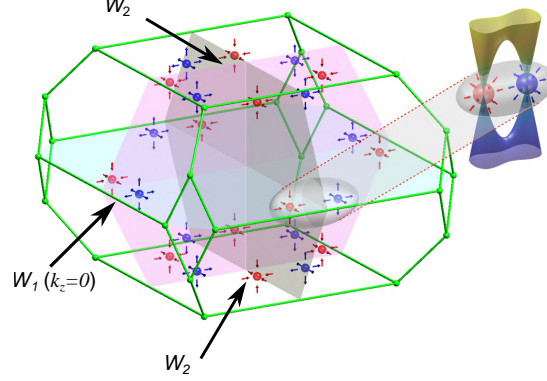


FIG. S2. Weyl points in the Brillouin zone of TaAs with one elementary Weyl pair highlighted. Adapted from Ref. [3].

The crystal structure consists of interpenetrating Ta and As sublattices, with two Ta atoms and two As atoms in each primitive unit cell. In Fig. S1(a), we show the BZ of TaAs with high-symmetry points and path. The energy bands (black curves), obtained by self consistent calculation without and with SOC, along the high-symmetry path are shown in Figs. S1(b) and (c), respectively. The corresponding density of states (DOSs) are plotted in Fig. S1(d).

To study the ultrafast dynamics in TaAs under a strong laser field, the tight-binding Hamiltonian ($\hat{H}_{\text{WF}}^{\mathbf{k}}$) and non-Abelian Berry connection ($\hat{\mathbf{D}}_{\text{WF}}^{\mathbf{k}}$) are constructed by projecting the Hamiltonian and position operator onto localized Wannier functions $|\mathbf{R}n\rangle$, respectively

$$(\hat{H}_{\text{WF}}^{\mathbf{k}})_{nm} = \sum_{\mathbf{R}} e^{i\mathbf{k}\cdot\mathbf{R}} \langle \mathbf{0}n | \hat{H}_0 | \mathbf{R}m \rangle, \quad (\text{S1})$$

$$(\hat{\mathbf{D}}_{\text{WF}}^{\mathbf{k}})_{nm} = \sum_{\mathbf{R}} e^{i\mathbf{k}\cdot\mathbf{R}} \langle \mathbf{0}n | \hat{\mathbf{r}} | \mathbf{R}m \rangle, \quad (\text{S2})$$

where \mathbf{R} sums over all the lattice vectors. The Wannier tight-binding model comprises the Ta-5d, 6s and As-4p orbitals, with energy window lying between -7.5 eV and $+6.2$ eV. Therefore, the basis set for the Wannier projections consists of 18 orbitals for the scalar relativistic case (without SOC). Correspondingly, the basis of Wannier functions involved 36 orbitals when spin-orbit interactions were considered. The energy bands (red curves), by Wannier fit, are depicted on the top of DFT bands, as illustrated in Figs. S1(b) and S1(c).

The Weyl points (WPs) in BZ are searched and confirmed by computing the Chern numbers as implemented in PYFLO module of the FPLO code, and outlined in Ref. [4]. We find 24 WPs in TaAs: 8 WPs (W_1) situated on the $k_z = 0$ plane, and 16 WPs (W_2) located away from the $k_z = 0$ plane, as shown in Fig. S2. The coordinates, chirality, and energies of WPs in TaAs are listed in Table S1.

B. Time evolution method for Wannier Hamiltonian

To simulate the interaction between the laser field and the system, we solve the time-dependent Schrödinger equation using the velocity gauge within the pseudo-Houston representation [5]. This approach employs an accelerated Bloch-like basis formed by maximally localized Wannier functions

$$i \frac{\partial}{\partial t} |m, \mathbf{k}_0, t\rangle = \left[\hat{H}_{\text{WF}}^{\mathbf{k}(t)} + \mathbf{F}(t) \cdot \hat{\mathbf{D}}_{\text{WF}}^{\mathbf{k}(t)} \right] |m, \mathbf{k}_0, t\rangle, \quad (\text{S3})$$

where m is the band index. The quasi-momentum is $\mathbf{k}(t) = \mathbf{k}_0 + \mathbf{A}(t)$, with \mathbf{k}_0 being the initial quasi-momentum. The vector potential $\mathbf{A}(t)$ of laser field is expressed as

$$\mathbf{A}(t) = \frac{E_0}{\omega_0} f(t) \left[\frac{1}{\sqrt{1+\epsilon^2}} \cos(\omega_0 t + \phi) \mathbf{e}_x + \frac{\epsilon}{\sqrt{1+\epsilon^2}} \sin(\omega_0 t + \phi) \mathbf{e}_y \right], \quad (\text{S4})$$

where E_0 is the peak electric field, $f(t) = \sin^2(\omega_0 t/2n_{\text{cyc}})$ is the envelope, ω_0 is the fundamental frequency, ϵ is the ellipticity, ϕ is the carrier envelope phase, and n_{cyc} is the total number of laser cycles. The corresponding electric field is $\mathbf{F}(t) = -d\mathbf{A}(t)/dt$. We omit $\hat{\mathbf{D}}_{\text{WF}}^{\mathbf{k}(t)}$ in this work, because it only has a minor influence on high-harmonic generation [5].

The wave functions of all occupied states are propagated independently by repetitively applying the time evolution operator until the end of the laser pulse

$$|m, \mathbf{k}_0, t + \Delta t\rangle = \hat{U}(t, t + \Delta t, \mathbf{k}_0) |m, \mathbf{k}_0, t\rangle. \quad (\text{S5})$$

Here, the time evolution operator is evaluated by

$$\hat{U}(t, t + \Delta t, \mathbf{k}_0) = \sum_n |n, \mathbf{k}(t)\rangle e^{-i\lambda_n[\mathbf{k}(t)]\Delta t} \langle n, \mathbf{k}(t)|, \quad (\text{S6})$$

where $\lambda_n[\mathbf{k}(t)]$ and $|n, \mathbf{k}(t)\rangle$ are the eigenvalues and eigenstates of the time-dependent Hamiltonian $\hat{H}_{\text{WF}}^{\mathbf{k}(t)}$. The time-dependent current reads

$$\mathbf{J}(t) = \int_{\text{BZ}} [d\mathbf{k}_0] \sum_m \langle m, \mathbf{k}_0, t | \hat{\mathbf{p}}[\mathbf{k}(t)] | m, \mathbf{k}_0, t \rangle, \quad (\text{S7})$$

where $\int [d\mathbf{k}_0]$ denotes $\int d^d k_0 / (2\pi)^d$, and d indicates the dimension of system. The momentum operator in the pseudo-Houston representation [6] reads

$$\hat{\mathbf{p}} = \nabla_{\mathbf{k}} \hat{H}_{\text{WF}}^{\mathbf{k}(t)} + i[\hat{H}_{\text{WF}}^{\mathbf{k}(t)}, \hat{\mathbf{D}}_{\text{WF}}^{\mathbf{k}(t)}], \quad (\text{S8})$$

where $[\hat{H}_{\text{WF}}^{\mathbf{k}(t)}, \hat{\mathbf{D}}_{\text{WF}}^{\mathbf{k}(t)}]$ represents the commutation of the Hamiltonian and position operator, and is omitted as mentioned above. The HHG spectrum is computed by

$$I_l(\omega) = \left| \int dt e^{-i\omega t} W(t) \frac{d}{dt} J_l(t) \right|^2, \quad (\text{S9})$$

where $l = x, y, z$ indicates the direction index, and $W(t)$ denotes the Blackman window function. For the integral of Eq. (S7), the BZ is sampled by k grids from $20 \times 20 \times 20$ to $100 \times 100 \times 100$. Satisfactory convergence is achieved for a k grid of size $50 \times 50 \times 50$ for HHG spectra.

C. Formulas of HHG ellipticity and HHG circular dichroism

The vector potential [Eq. (S4)] represents a right-handed circularly polarized (RCP) field when $\epsilon = -1$, while it indicates a left-handed circularly polarized (LCP) field when $\epsilon = +1$. If we take into account the complex amplitude of vector potential, the LCP field obeys $A_y/A_x = -i$ while the RCP field obeys $A_y/A_x = i$.

The ellipticity of harmonic emission reads

$$\epsilon_n = \frac{\sqrt{I_n^{(+)} - I_n^{(-)}}}{\sqrt{I_n^{(+)} + I_n^{(-)}}}, \quad (\text{S10})$$

where $I_n^{(\pm)} = (n\omega)^2 |J_x(n\omega) \pm iJ_y(n\omega)|^2$ represents the intensity of harmonic field projected into two orthogonal (\pm) circularly polarized basis sets. The circular dichroism is defined in terms of the circular components $I_{n,v}^{(\pm)}$

$$\text{CD}_n = \frac{I_{n,\text{RCP}}^{(+)} - I_{n,\text{LCP}}^{(-)}}{I_{n,\text{RCP}}^{(+)} + I_{n,\text{LCP}}^{(-)}}, \quad (\text{S11})$$

where $v = \text{RCP/LCP}$ in $I_{n,v}^{(\pm)}$ denotes the polarization state of driving fields.

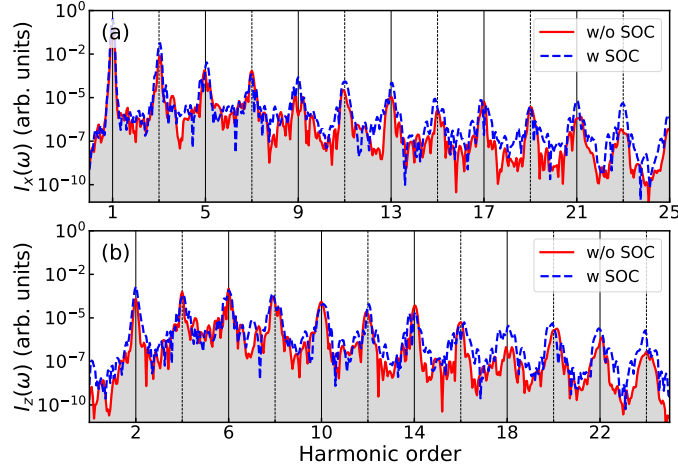


FIG. S3. HHG spectra in TaAs without and with SOC driven by a linearly polarized (LP) pulse. (a) HHG in x direction $I_x(\omega)$ and (b) HHG in z direction $I_z(\omega)$. The red and blue curves represent harmonic spectra in TaAs with SOC and without SOC, respectively. The laser is polarized along the x axis with intensity $I_0 = 5.04 \times 10^{10}$ W/cm² ($E_0 = 0.0012$ a.u.), wavelength $\lambda = 4200$ nm ($\hbar\omega = 0.295$ eV), and a duration of 20 cycles.

II. EFFECT OF SOC

Our DFT calculations consider two scenarios: the scalar relativistic approximation (without SOC) and the full relativistic correction (with SOC), because the SOC is expected to play a crucial role in determining the properties of topological materials. In topological insulators, the absence of SOC can result in a trivial insulator or a Dirac semimetal phase (e.g., as in Bi₂Se₃, Bi₂Te₃, 1T'-MoS₂, 1T'-WTe₂, and so forth). Activating SOC modifies the band gap and gives rise to a distinct topological phase, significantly influencing the harmonic emissions.

However, the HHG in TaAs shows relatively minor effect from SOC, as observed in the comparison of the red and blue curves in Figs. S3(a)-(b). This is because SOC leads to only slight alterations in the band structure and DOSs in TaAs, as illustrated in Figs. S1(b)-(d). Note that the influence of SOC has been considered in all calculations in the main text unless otherwise stated.

III. JONES MATRIX FORMALISM

A. Eigenvalue problems: the structural symmetry of the Hamiltonian

Let $\hat{\mathcal{O}}$ be an operation of space group symmetry defined by a combination of translation (a fractional lattice vector) and orthogonal transformation $\hat{\mathcal{R}}$. The scalar $f(\mathbf{r})$ function is transformed by

$$\hat{\mathcal{O}}f(\mathbf{r}) = f(\mathcal{R}^{-1}\mathbf{r} - \mathcal{R}^{-1}\frac{a_j}{M}), \quad (\text{S12})$$

where \mathcal{R} is the matrix representation of orthogonal transformation ($\hat{\mathcal{R}}$), a_j indicates the j th lattice vector, and M is an integer number.

The eigenvalue problem of periodic part of Bloch states is

$$\hat{H}(\mathbf{k})|n, \mathbf{k}\rangle = E_n^{\mathbf{k}}|n, \mathbf{k}\rangle \quad (\text{S13})$$

with the Hamiltonian

$$\hat{H}(\mathbf{k}) = \frac{\hat{\mathbf{p}}^2}{2} + \frac{\mathbf{k}^2}{2} + \mathbf{k} \cdot \hat{\mathbf{p}} + \hat{V}, \quad (\text{S14})$$

where $\hat{\mathbf{p}}$ is the momentum operator, \hat{V} is the potential operator, and $E_n^{\mathbf{k}}$ is the eigenvalue of the state $|n, \mathbf{k}\rangle$. If the

system is invariant under a space group transformation, the operator $\hat{\mathcal{O}}$ commutes with the Hamiltonian:

$$\begin{aligned}
\hat{\mathcal{O}}\hat{H}(\mathbf{k})\hat{\mathcal{O}}^{-1} &= \frac{\hat{\mathbf{p}}^2}{2} + \frac{\mathbf{k}^2}{2} + \mathbf{k} \cdot \hat{\mathcal{O}}\hat{\mathbf{p}}\hat{\mathcal{O}}^{-1} + \hat{V} \\
&= \frac{\hat{\mathbf{p}}^2}{2} + \frac{\mathbf{k}^2}{2} + \mathbf{k} \cdot \hat{\mathcal{R}}\hat{\mathbf{p}}\hat{\mathcal{R}}^{-1} + \hat{V} \\
&= \frac{\hat{\mathbf{p}}^2}{2} + \frac{(\mathcal{R}\mathbf{k})^2}{2} + \mathcal{R}^{-1}(\mathcal{R}\mathbf{k}) \cdot \mathcal{R}^{-1}\hat{\mathbf{p}} + \hat{V} \\
&= \hat{H}(\mathcal{R}\mathbf{k}).
\end{aligned} \tag{S15}$$

Here we have considered

$$\begin{aligned}
\hat{\mathcal{R}}\hat{\mathbf{p}}\hat{\mathcal{R}}^{-1}f(\mathbf{r}) &= -\hat{\mathcal{R}}i\nabla_{\mathbf{r}}f(\mathcal{R}\mathbf{r}) \\
&= -\hat{\mathcal{R}}\mathcal{R}^{-1}i\nabla_{\mathcal{R}\mathbf{r}}f(\mathcal{R}\mathbf{r}) \\
&= -\mathcal{R}^{-1}i\left[\hat{\mathcal{R}}f_x(\mathcal{R}\mathbf{r}), \hat{\mathcal{R}}f_y(\mathcal{R}\mathbf{r}), \hat{\mathcal{R}}f_z(\mathcal{R}\mathbf{r})\right]^T \\
&= \mathcal{R}^{-1}\hat{\mathbf{p}}f(\mathbf{r})
\end{aligned} \tag{S16}$$

and the dot product of any two vectors is invariant under the orthogonal transformation. Applying $\hat{\mathcal{O}}$ to the two side of Eq. (S13), we find

$$\begin{aligned}
\hat{\mathcal{O}}\hat{H}(\mathbf{k})|n, \mathbf{k}\rangle &= \hat{\mathcal{O}}\hat{H}(\mathbf{k})\hat{\mathcal{O}}^{-1}\hat{\mathcal{O}}|n, \mathbf{k}\rangle \\
&= \hat{H}(\mathcal{R}\mathbf{k})\hat{\mathcal{O}}|n, \mathbf{k}\rangle \\
&= E_n^{\mathbf{k}}\hat{\mathcal{O}}|n, \mathbf{k}\rangle.
\end{aligned} \tag{S17}$$

Due to $\hat{\mathcal{O}}|n, \mathbf{k}\rangle$ is the eigenstate of $\hat{H}(\mathcal{R}\mathbf{k})$ with the eigenvalue $E_n^{\mathbf{k}}$, the eigenvalue and eigenstate satisfy

$$\begin{aligned}
E_n^{\mathbf{k}} &= E_n^{\mathcal{R}\mathbf{k}}, \\
\hat{\mathcal{O}}|n, \mathbf{k}\rangle &= |n, \mathcal{R}\mathbf{k}\rangle e^{i\phi_n^{\mathcal{R}\mathbf{k}}},
\end{aligned} \tag{S18}$$

where $\phi_n^{\mathcal{R}\mathbf{k}}$ is a gauge dependent phase factor.

B. Jones matrix for HHG under structural symmetry

In this section, our goal is to derive the Jones matrix for HHG (from crystalline solids) in the following form

$$\mathcal{J}(n_H) = \sum_{l'=1}^{N'} (\mathcal{R}')^{l'} \sum_{l=1}^N \exp(-i2\pi n_H \frac{l}{N}) (\mathcal{R})^l, \tag{S19}$$

where n_H is the harmonic order, \mathcal{R} and \mathcal{R}' are the shared orthogonal transformations of external field and crystal structure, N and N' are respectively the orders of symmetry elements \mathcal{R} and \mathcal{R}' [$\mathcal{R}^N = E$, $(\mathcal{R}')^N = E$], and E is the identity element. In the following derivation, we explain the difference of \mathcal{R} and \mathcal{R}' .

We start our derivation here. Using Eq. (S7), the amplitude of the n_H th harmonic is expressed as

$$\mathcal{J}(n_H\omega_0) = \sum_{E_n^{\mathbf{k}} \leq \varepsilon_F} \int_{\text{BZ}} [d\mathbf{k}_0] \int_{-\infty}^{+\infty} dt \langle n, \mathbf{k}_0, t_0 | \hat{U}^\dagger(\mathbf{k}_0, t, t_0) [\hat{\mathbf{p}} + \mathbf{k}_0 + \mathbf{A}(t)] \hat{U}(\mathbf{k}_0, t, t_0) | n, \mathbf{k}_0, t_0 \rangle e^{-in_H\omega_0 t}, \tag{S20}$$

where ε_F is the Fermi energy, time evolution operator reads

$$\hat{U}(\mathbf{k}_0, t, t_0) = \hat{\mathcal{T}} e^{-i \int_{t_0}^t d\tau \hat{H}[\mathbf{k}_0 + \mathbf{A}(\tau)]}, \tag{S21}$$

and $\hat{\mathcal{T}}$ is the time ordering operator. The generation of a specific harmonic is determined by the shared symmetries of the laser field and the lattice. These shared symmetries are classified into two categories in the following discussion:

i) where the laser field under the symmetry operation can be transformed into the operation of temporal translation, and ii) where the laser field remains unchanged under the symmetry operation.

First, we discuss the case i). We neglect $\mathbf{k}_0 + \mathbf{A}(t)$ in Eq. (S20) because it only contributes to the first order harmonic. The space group operation $\hat{\mathcal{O}}$ [defined by Eq. (S12)] is equivalent to the orthogonal transformation \mathcal{R} when applying to an external field. The external field is translated by lT_0/N in time

$$\mathcal{R}^l \mathbf{A}(t) = \mathbf{A}(t + lT_0/N), \quad (\text{S22})$$

when it is operated by the l th order of \mathcal{R} , where $T_0 = 2\pi/\omega_0$ is the period of laser field. For the time-dependent Hamiltonian and time evolution operator [using Eq. (S15)], we have

$$\hat{H}[\mathbf{k}_0 + \mathbf{A}(\tau + lT_0/N)] = \hat{H}[\mathcal{R}^l \mathcal{R}^{-1} \mathbf{k}_0 + \mathcal{R}^l \mathbf{A}(\tau)] = \hat{\mathcal{O}}^l \hat{H}(\mathcal{R}^{-l} \mathbf{k}_0, \tau) \hat{\mathcal{O}}^{-l}, \quad (\text{S23})$$

and

$$\hat{U}(\mathbf{k}_0, t + lT_0/N, t_0 + lT_0/N) = \hat{\mathcal{O}}^l \hat{U}(\mathcal{R}^{-l} \mathbf{k}_0, t, t_0) \hat{\mathcal{O}}^{-l}. \quad (\text{S24})$$

Equation (S24) allows us to reduce the integral over the entire time domain to $[0, T_0/N]$. The whole integral can be transferred into the summation of small intervals by $\int_{-\infty}^{\infty} dt \rightarrow \sum_m \sum_{l=1}^N \int_{mT_0+(l-1)T_0/N}^{mT_0+lT_0/N} dt$. Thus, equation (S20) can be rewritten by

$$\begin{aligned} \mathbf{J}(n_H \omega_0) = & \sum_{E_n^{\mathbf{k}} \leq \varepsilon_F} \sum_m \sum_{l=1}^N \int_{\text{BZ}} [d\mathbf{k}_0] \int_{mT_0+(l-1)T_0/N}^{mT_0+lT_0/N} dt \\ & \langle n, \mathbf{k}_0, t_0 | \hat{U}^\dagger(\mathbf{k}_0, t, t_0) \hat{\mathbf{p}} \hat{U}(\mathbf{k}_0, t, t_0) | n, \mathbf{k}_0, t_0 \rangle e^{-in_H \omega_0 t}. \end{aligned} \quad (\text{S25})$$

Let $t_0 = mT_0 + (l-1)T_0/N$, the n_H th harmonic field becomes

$$\begin{aligned} \mathbf{J}(n_H \omega_0) = & \sum_{E_n^{\mathbf{k}} \leq \varepsilon_F} \sum_m \sum_{l=1}^N \int_{\text{BZ}} [d\mathbf{k}_0] \int_0^{T_0/N} dt e^{-in_H \omega_0 t - in_H(l-1)2\pi/N} \\ & \langle n, \mathbf{k}_0, mT_0 + (l-1)T_0/N | \hat{U}^\dagger(\mathbf{k}_0, t + (l-1)T_0/N, (l-1)T_0/N) \\ & \hat{\mathbf{p}} \hat{U}(\mathbf{k}_0, t + (l-1)T_0/N, (l-1)T_0/N) | n, \mathbf{k}_0, mT_0 + (l-1)T_0/N \rangle, \end{aligned} \quad (\text{S26})$$

by considering $\int_{mT_0+(l-1)T_0/N}^{mT_0+lT_0/N} f(t)dt = \int_0^{T_0/N} f[t + mT_0 + (l-1)T_0/N]dt$ and $\hat{U}(\mathbf{k}_0, t + mT_0, t_0 + mT_0) = \hat{U}(\mathbf{k}_0, t, t_0)$. Substituting Eqs. (S22) and (S24) into Eq. (S26), we obtain

$$\begin{aligned} \mathbf{J}(n_H \omega_0) = & \sum_{E_n^{\mathbf{k}} \leq \varepsilon_F} \sum_m \sum_{l=1}^N \int_{\text{BZ}} [d\mathbf{k}_0] \int_0^{T_0/N} dt e^{-in_H \omega_0 t - in_H(l-1)2\pi/N} \\ & \langle n, \mathbf{k}_0, mT_0 + (l-1)T_0/N | \hat{\mathcal{O}}^{(l-1)} \hat{U}^\dagger(\mathcal{R}^{-(l-1)} \mathbf{k}_0, t, 0) \hat{\mathcal{O}}^{-(l-1)} \\ & \hat{\mathbf{p}} \hat{\mathcal{O}}^{(l-1)} \hat{U}(\mathcal{R}^{-(l-1)} \mathbf{k}_0, t, 0) \hat{\mathcal{O}}^{-(l-1)} | n, \mathbf{k}_0, mT_0 + (l-1)T_0/N \rangle. \end{aligned} \quad (\text{S27})$$

Assuming the low excitation of valence electrons, we can roughly think that the wave function propagates adiabatically on the valence bands

$$|n, \mathbf{k}_0, mT_0 + (l-1)T_0/N\rangle \approx |n, \mathbf{k}_0 + \mathbf{A}[mT_0 + (l-1)T_0/N]\rangle e^{i\phi_n^{\mathbf{k}_0}[mT_0+(l-1)T_0/N]}. \quad (\text{S28})$$

Substituting Eqs.(S16), (S18), (S22) and (S28) into Eq. (S27), we have

$$\begin{aligned} \mathbf{J}(n_H \omega_0) = & \sum_{l=1}^N \mathcal{R}^{(l-1)} e^{-in_H(l-1)2\pi/N} \sum_{n, m} \int_{\text{BZ}} [d\mathbf{k}'_0] \int_0^{T_0/N} dt e^{-in_H \omega_0 t} \\ & \langle n, \mathbf{k}'_0 + \mathbf{A}(0) | \hat{U}^\dagger(\mathbf{k}'_0, t, 0) \hat{\mathbf{p}} \hat{U}(\mathbf{k}'_0, t, 0) | n, \mathbf{k}'_0 + \mathbf{A}(0) \rangle, \end{aligned} \quad (\text{S29})$$

where $\mathcal{R}^{-(l-1)} \mathbf{k}_0$ is replaced by \mathbf{k}'_0 .

Then we consider case ii): the laser field is invariant under the operator $\hat{\mathcal{O}}'$. The vector potential of the laser field satisfies

$$\mathbf{A}(t) = \mathcal{R}' \mathbf{A}(t), \quad (\text{S30})$$

and the potential operator satisfies

$$\hat{V} = \hat{\mathcal{O}}'^l \hat{V} \hat{\mathcal{O}}'^{-l}. \quad (\text{S31})$$

We give some specific examples of this case in the next section. Using Eqs. (S15), we immediately have

$$\hat{U}(\mathcal{R}'^l \mathbf{k}_0, t, t_0) = \hat{\mathcal{O}}'^l \hat{U}(\mathbf{k}_0, t, t_0) \hat{\mathcal{O}}'^{-l}, \quad (\text{S32})$$

and

$$\begin{aligned} & \left\langle n, \mathcal{R}'^l \mathbf{k}'_0 + \mathbf{A}(0) \right| \hat{U}^\dagger(\mathcal{R}'^l \mathbf{k}'_0, t, 0) \hat{\mathbf{p}} \hat{U}(\mathcal{R}'^l \mathbf{k}'_0, t, 0) \left| n, \mathcal{R}'^l \mathbf{k}'_0 + \mathbf{A}(0) \right\rangle \\ &= \left\langle n, \mathbf{k}'_0 + \mathbf{A}(0) \right| \hat{U}^\dagger(\mathbf{k}'_0, t, 0) \hat{\mathcal{O}}'^{-l} \hat{\mathbf{p}} \hat{\mathcal{O}}'^l \hat{U}(\mathbf{k}'_0, t, 0) \left| n, \mathbf{k}'_0 + \mathbf{A}(0) \right\rangle \\ &= \mathcal{R}'^l \left\langle n, \mathbf{k}'_0 + \mathbf{A}(0) \right| \hat{U}^\dagger(\mathbf{k}'_0, t, 0) \hat{\mathbf{p}} \hat{U}(\mathbf{k}'_0, t, 0) \left| n, \mathbf{k}'_0 + \mathbf{A}(0) \right\rangle. \end{aligned} \quad (\text{S33})$$

Plugging Eq. (S33) into (S29), the integral over the entire first BZ converts to the integral over an irreducible Brillouin zone (BZ'). Therefore the n_H th harmonic field is expressed by

$$\mathbf{J}(n_H \omega_0) = \mathcal{J}(n_H) \mathbf{J}^{\text{ir}}(n_H \omega_0), \quad (\text{S34})$$

where

$$\mathcal{J}(n_H) = \sum_{l'=1}^{N'} \mathcal{R}'^{l'} \sum_{l=1}^N \mathcal{R}^{(l-1)} e^{-in_H(l-1)2\pi/N} \quad (\text{S35})$$

and

$$\mathbf{J}^{\text{ir}}(n_H \omega_0) = \sum_{n,m} \int_{\text{BZ}'} [d\mathbf{k}'_0] \int_0^{T_0/N} dt e^{-in_H \omega_0 t} \left\langle n, \mathbf{k}'_0 + \mathbf{A}(0) \right| \hat{U}^\dagger(\mathbf{k}'_0, t, 0) \hat{\mathbf{p}} \hat{U}(\mathbf{k}'_0, t, 0) \left| n, \mathbf{k}'_0 + \mathbf{A}(0) \right\rangle. \quad (\text{S36})$$

We surprisingly find that $\mathcal{J}(n_H)$ which induced by the structural symmetries is just the Jones matrix extensively used in the classic optics [7]. It determines the allowed orders and the polarization states of HHG. Moreover, $\mathbf{J}^{\text{ir}}(n_H \omega_0)$ is the irreducible part of n_H th harmonic field and can be treated as a Jones vector.

One may note that shifting the summation range with respect to l does not change the summation result in Eq. (S35). Thus we can convert Eq. (S35) to Eq. (S19).

C. Examples of applying Jones matrix to TaAs HHG

In this section, we use Jones matrix [Eq. (S19)] to provide a detailed explanation of the selection rule for TaAs HHG shown in main text. Then we give an extra example of HHG excited by LP laser along z direction.

1. LP driver in x - y plane

Firstly, we focus on the case where the laser is linearly polarized along the x direction as shown in Fig. S4(a). We find that the shared symmetries are $\mathcal{R} = \mathcal{C}_{2(z)}$ and $\mathcal{R}' = \mathcal{M}_y$. The vector potential $\mathbf{A}(t)$ is shifted by $T_0/2$ in time by the operation of $\mathcal{C}_{2(z)}$ but is invariant under the operation of \mathcal{M}_y . The matrix representation of shared symmetries are

$$\mathcal{R} = \mathcal{C}_{2(z)} = \begin{pmatrix} -1 & & \\ & -1 & \\ & & 1 \end{pmatrix} \text{ and } \mathcal{R}' = \mathcal{M}_y = \begin{pmatrix} 1 & & \\ & -1 & \\ & & 1 \end{pmatrix}, \quad (\text{S37})$$

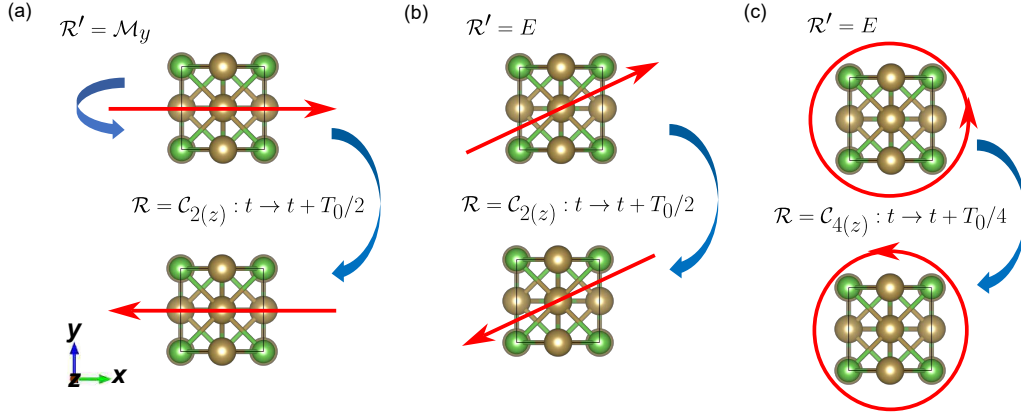


FIG. S4. Sketch illustrating the interaction of laser field and TaAs lattice under operation of crystal symmetry.

where $\mathcal{C}_{2(z)}(x, y, z)^T = (-x, -y, z)^T$ and $\mathcal{M}_y(x, y, z)^T = (x, -y, z)^T$. Plugging Eq. (S37) into Eq. (S19), the corresponding Jones matrix is

$$\mathcal{J}(n_H) = 2 \begin{pmatrix} 1 - e^{-i\pi n_H} & 0 \\ 0 & 1 + e^{-i\pi n_H} \end{pmatrix}. \quad (\text{S38})$$

Therefore, both odd ($n_H = 2k + 1$) and even ($n_H = 2k$) harmonics are allowed according to Eq. (S38), where $k \in \mathbb{N}$. The Jones matrix for odd harmonics is

$$\mathcal{J}(n_H = 2k + 1) = 4 \begin{pmatrix} 1 & 0 \\ 0 & 0 \end{pmatrix}, \quad (\text{S39})$$

while the Jones matrix for even harmonics is

$$\mathcal{J}(n_H = 2k) = 4 \begin{pmatrix} 0 & 0 \\ 0 & 1 \end{pmatrix}. \quad (\text{S40})$$

From the perspective of classic optics, $\mathcal{J}(2k + 1)$ is just a linear polarizer with an axis along x , while $\mathcal{J}(2k)$ serves as a linear polarizer with an axis along z . Applying Jones matrices to the corresponding Jones vectors, we find

$$\begin{aligned} \mathbf{J}[(2k + 1)\omega_0] &= \mathcal{J}(2k + 1)\mathbf{J}^{ir} \\ &= \begin{pmatrix} 1 & 0 \\ 0 & 0 \end{pmatrix} \begin{pmatrix} J_x^{ir} \\ J_y^{ir} \\ J_z^{ir} \end{pmatrix} = J_x^{ir}[(2k + 1)\omega_0]\mathbf{e}_x, \end{aligned} \quad (\text{S41})$$

and

$$\begin{aligned} \mathbf{J}[(2k)\omega_0] &= \mathcal{J}(2k)\mathbf{J}^{ir} \\ &= \begin{pmatrix} 0 & 0 \\ 0 & 1 \end{pmatrix} \begin{pmatrix} J_x^{ir} \\ J_y^{ir} \\ J_z^{ir} \end{pmatrix} = J_z^{ir}[(2k)\omega_0]\mathbf{e}_z. \end{aligned} \quad (\text{S42})$$

The prefactors “4” in Jones matrices are absorbed into the Jones vectors. In the following derivation, the prefactors in Jones matrices are all ignored unless otherwise stated. Equations (S41) and (S42) imply that the linearly polarized odd harmonics are permitted in the x direction while the linearly polarized even harmonics are allowed in the z direction. This is consistent with our observations in the main text.

Then we consider the LP field deviates from high symmetry axes (like x axis) shown in Fig. S4(b). The shared symmetries are

$$\mathcal{R} = \mathcal{C}_{2(z)} = \begin{pmatrix} -1 & & \\ & -1 & \\ & & 1 \end{pmatrix} \text{ and } \mathcal{R}' = E = \begin{pmatrix} 1 & & \\ & 1 & \\ & & 1 \end{pmatrix}. \quad (\text{S43})$$

Substituting Eq. (S43) into Eq. (S19), the Jones matrix is

$$\mathcal{J}(n_H) = \begin{pmatrix} 1 - e^{-i\pi n_H} & & \\ & 1 - e^{-i\pi n_H} & \\ & & 1 + e^{-i\pi n_H} \end{pmatrix}. \quad (\text{S44})$$

We thus find that the odd harmonics are allowed in both x and y directions, because the corresponding Jones matrix reads

$$\mathcal{J}(n_H = 2k + 1) = \begin{pmatrix} 1 & & \\ & 1 & \\ & & 0 \end{pmatrix}. \quad (\text{S45})$$

The odd harmonic field is expressed by

$$\begin{aligned} \mathbf{J}[(2k + 1)\omega_0] &= \mathcal{J}(2k + 1)\mathbf{J}^{ir} \\ &= \begin{pmatrix} 1 & & \\ & 1 & \\ & & 0 \end{pmatrix} \begin{pmatrix} J_x^{ir} \\ J_y^{ir} \\ J_z^{ir} \end{pmatrix} \\ &= \begin{pmatrix} J_x^{ir} \\ J_y^{ir} \\ 0 \end{pmatrix}. \end{aligned} \quad (\text{S46})$$

Since J_x^{ir} and J_y^{ir} are generally nonzero, the odd harmonics are elliptically polarized. This is verified by Fig. S7(d). We can observe the nonzero harmonic ellipticity when the LP laser deviates from high symmetry axes. Nevertheless, the even harmonics is still linearly polarized, due to

$$\mathcal{J}(n_H = 2k) = \begin{pmatrix} 0 & & \\ & 0 & \\ & & 1 \end{pmatrix}. \quad (\text{S47})$$

2. LCP driver in x - y plane

Then we analyze the TaAs interacting with LCP laser, as shown in Fig. S4(c). The shared symmetries are

$$\mathcal{R} = \mathcal{C}_{4(z)} = \begin{pmatrix} 0 & -1 & 0 \\ 1 & 0 & 0 \\ 0 & 0 & 1 \end{pmatrix} \text{ and } \mathcal{R}' = E = \begin{pmatrix} 1 & & \\ & 1 & \\ & & 1 \end{pmatrix}, \quad (\text{S48})$$

where $\mathcal{C}_{4(z)}(x, y, z)^T = (-y, x, z)^T$. Plugging Eq. (S48) into Eq. (S19), the Jones matrix is

$$\mathcal{J}(n_H) = \begin{pmatrix} 1 - e^{-i\pi n_H} & 2i \sin(\frac{\pi}{2} n_H) & 0 \\ -2i \sin(\frac{\pi}{2} n_H) & 1 - e^{-i\pi n_H} & 0 \\ 0 & 0 & (1 + i^{n_H})[1 + (-1)^{n_H}] \end{pmatrix}. \quad (\text{S49})$$

Therefore, the permitted harmonic orders are $n_H = 4k + 1$, $4k - 1$, and $4k$, and the corresponding Jones matrices have the forms of

$$\mathcal{J}(n_H = 4k \pm 1) = \begin{pmatrix} \frac{1}{2} & \pm \frac{i}{2} & 0 \\ \mp \frac{i}{2} & \frac{1}{2} & 0 \\ 0 & 0 & 0 \end{pmatrix} \quad (\text{S50})$$

and

$$\mathcal{J}(n_H = 4k) = \begin{pmatrix} 0 & & \\ & 0 & \\ & & 1 \end{pmatrix}. \quad (\text{S51})$$

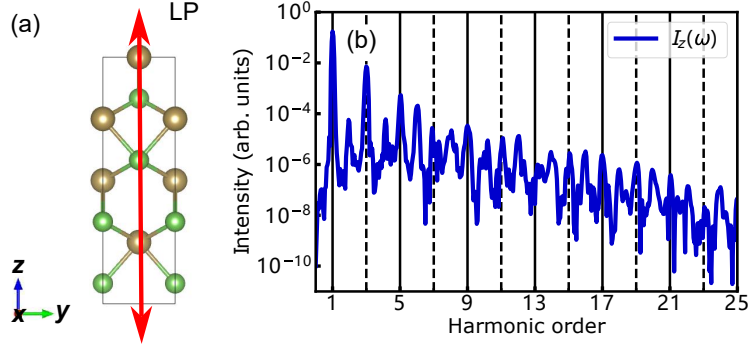


FIG. S5. (a) Sketch of LP laser polarized along the z axis of TaAs lattice. (b) Harmonic spectrum in the z direction. The laser parameters are the same as those in Fig. S3.

As we know, $\mathcal{J}(n_H = 4k)$ is a linear polarizer which only allows $(4k)$ th linearly polarized harmonics along the z direction. The Jones matrix $\mathcal{J}(n_H = 4k + 1)$ is a left circular polarizer, while $\mathcal{J}(n_H = 4k - 1)$ represents a right circular polarizer. Equation (S50) results in left-handed circularly polarized $(4k + 1)$ th harmonics in the x - y plane, because

$$\mathbf{J}[(4k + 1)\omega_0] = \mathcal{J}(4k + 1)\mathbf{J}^{ir} = \frac{1}{2} \begin{pmatrix} J_x^{ir} + iJ_y^{ir} \\ -iJ_x^{ir} + J_y^{ir} \\ 0 \end{pmatrix}, \quad (\text{S52})$$

and

$$\frac{J_y(4k + 1)}{J_x(4k + 1)} = \frac{-iJ_x^{ir} + J_y^{ir}}{J_x^{ir} + iJ_y^{ir}} = -i. \quad (\text{S53})$$

Nevertheless, the $(4k - 1)$ th harmonics are right-handed circularly polarized, because

$$\mathbf{J}[(4k - 1)\omega_0] = \mathcal{J}(4k - 1)\mathbf{J}^{ir} = \frac{1}{2} \begin{pmatrix} J_x^{ir} - iJ_y^{ir} \\ iJ_x^{ir} + J_y^{ir} \\ 0 \end{pmatrix}, \quad (\text{S54})$$

and

$$\frac{J_y(4k - 1)}{J_x(4k - 1)} = \frac{iJ_x^{ir} + J_y^{ir}}{J_x^{ir} - iJ_y^{ir}} = i. \quad (\text{S55})$$

These also agree with our observations in the main text.

3. LP driver along z axis

As the LP laser polarized along the z direction, we find that no crystal symmetry can result in a translation of the laser field in time. Thus the shared symmetry \mathcal{R} is E . However, the LP laser is invariant under the operation of \mathcal{M}_x , \mathcal{M}_y , \mathcal{M}_{xy} , \mathcal{M}_{-xy} , $\mathcal{C}_{2(z)}$, $\mathcal{C}_{4(z)}$, and $\mathcal{C}_{4-(z)}$, see Fig. S5(a). Plugging $\mathcal{R} = E$ and $\mathcal{R}' = \mathcal{M}_x, \mathcal{M}_y$ into Eq. (S19), the Jones matrix is expressed as

$$\mathcal{J}(n_H = k) = \begin{pmatrix} 0 & & \\ & 0 & \\ & & 1 \end{pmatrix}. \quad (\text{S56})$$

Equation (S56) indicates that both odd and even harmonics are permitted in the z direction, while harmonic emissions are prohibited in other directions. This is verified by the HHG spectrum shown in Fig. S5(b).

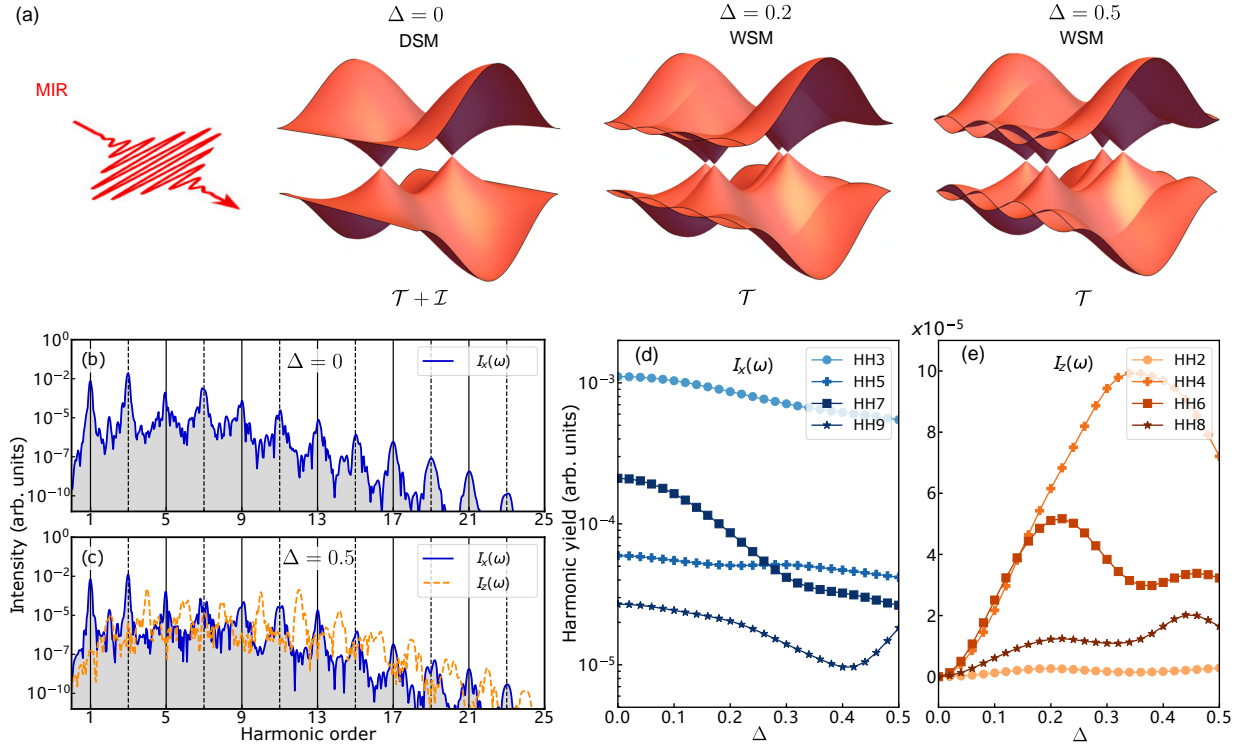


FIG. S6. (a) Band structure of minimal model for TaAs at $k_z = 0$ plane with different inversion symmetry parameters. HHG spectra for (b) $\Delta = 0$ and (c) $\Delta = 0.5$ driven by a linearly polarized field. Panels (d) and (e) show the yields of even- and odd-order harmonics as a function of inversion symmetry parameter Δ , respectively. Hamiltonian parameters are set to be $t = 0.8$ eV, $m_y = 1.0$, $m_z = 3.0$, and $a = 3.44$ Å. The laser intensity is $I_0 = 5.6 \times 10^{11}$ W/cm² ($E_0 = 0.004$ a.u.), and other laser parameters are the same as those in Fig. S3.

IV. ROLE OF INVERSION SYMMETRY BREAKING

In order to clarify the impact of \mathcal{I} breaking on HHG from TaAs, we utilize a four-band minimal model (\mathcal{T} is preserved) [8]

$$H_0(\mathbf{k}) = t\{\cos(k_x a) + m_y[1 - \cos(k_y a)] + m_z[1 - \cos(k_z a)]\}\sigma_x + t[\sin(k_y a) + \Delta \cos(k_y a)s_x]\sigma_y + t \sin(k_z a)s_x \sigma_z, \quad (\text{S57})$$

which supports four WPs in $k_z = 0$ plane capturing main physics near the Fermi energy. Here, σ_i and s_i denote Pauli matrices symbolizing the orbital and spin degrees of freedom, respectively. t is the hopping strength, a is the lattice constant, m_y and m_z are parameters that introduce anisotropy, and Δ introduces \mathcal{I} breaking. Roughly speaking, the larger the Δ , the greater the inversion symmetry is broken. This effective model preserves the $mm2$ point group, which is a subgroup of $4mm$ point group of crystal TaAs.

Firstly, we discuss the crystal symmetries in the model. For $\Delta = 0$, the model has \mathcal{I} , \mathcal{M}_x , \mathcal{M}_y , \mathcal{M}_z , $\mathcal{C}_{2(x)}$, $\mathcal{C}_{2(y)}$, and $\mathcal{C}_{2(z)}$ symmetries. It is worth to note that these symmetries are not independent, because $\mathcal{I} = \mathcal{M}_x \mathcal{M}_y \mathcal{M}_z = \mathcal{M}_z \mathcal{C}_{2(z)} = \mathcal{M}_x \mathcal{C}_{2(x)} = \mathcal{M}_y \mathcal{C}_{2(y)}$. For $\Delta \neq 0$, the Δ term breaks the \mathcal{M}_z symmetry, which naturally results in the absence of \mathcal{I} , $\mathcal{C}_{2(x)}$, and $\mathcal{C}_{2(y)}$. Only \mathcal{M}_x , \mathcal{M}_y , and $\mathcal{C}_{2(z)}$ symmetries are preserved. The broken \mathcal{M}_z is exactly the reason causes \mathcal{I} breaking in the realistic TaAs, as shown in Fig. S5(a).

Secondly, we focus on the HHG in the TaAs model. In the scenario where $\Delta = 0$, the exist of both \mathcal{T} and \mathcal{I} symmetries leads to a Dirac semimetal (DSM) phase. Two Dirac nodes emerge at $\mathbf{k} = (\pm\pi/2a, 0, 0)$ as illustrated in Fig. S6(a). Consequently, only odd harmonics are observable in the x direction when a LP pulse is applied along the x direction, as depicted in Fig. S6(b). With increasing Δ (breaking \mathcal{M}_z), the Dirac points split into pairs of WPs with opposite chirality and displace in opposite directions along the k_y axis ($\Delta k_y \propto \Delta/a$). In the case of $\Delta = 0.5$, as shown in Fig. S6(c), even harmonics appear in the z direction because of $\mathcal{C}_{2(z)}$ symmetry. In Figs. S6(d) and S6(e), we present how the yield of ordinary and anomalous harmonics varies with increasing the inversion breaking parameter Δ . Within the range ($\Delta < 0.2$) where the \mathcal{I} breaking term can be treated as a perturbation to the Hamiltonian, the yields of odd harmonics are suppressed while the yields of even harmonics increase monotonously. However, the

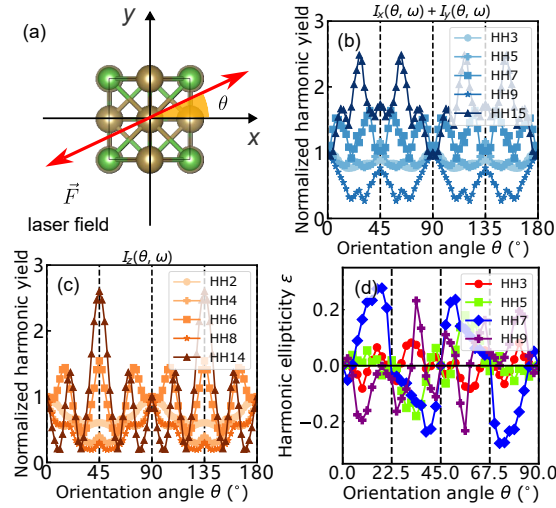


FIG. S7. (a) Sketch of the LP field and crystal structure, where θ is the angle of electric field relative to the x axis. (b) and (c) Normalized yields of the even- and odd-order harmonics vs orientation angle θ . (d) Ellipticity of emitted odd-order harmonics vs orientation angle. The laser parameters are the same as those in Fig. S3.

variation of harmonic yields deviates from a monotonic pattern, as Δ enters nonperturbation zone ($\Delta > 0.2$).

Finally, the Jones matrix formalism suggests that it is necessary to identify which sub-symmetry absence leads to the breaking of \mathcal{I} when focusing on the selection rule of HHG. In our case, the absence of \mathcal{M}_z results in odd harmonics in the x direction but even harmonics in the z direction when the laser is polarized along the x direction. However, both odd and even harmonics can be observed in the x and y directions in other systems if the broken \mathcal{I} stems from the absence of $\mathcal{C}_{2(z)}$. In the z direction, harmonic emission would not be allowed.

V. ORIENTATION DEPENDENCE

In Figs. S7(b) and S7(c), we find that the crystal symmetries of TaAs are reflected in the angular dependence of both ordinary (x - y plane) and anomalous harmonics (z direction). The $\mathcal{C}_{4(z)}$ and $\mathcal{C}_{4-(z)}$ strongly modulate the harmonic yields with a common period of 90° . The mirror symmetries (\mathcal{M}_x , \mathcal{M}_y , \mathcal{M}_{xy} , and \mathcal{M}_{-xy}) ensure the symmetric profiles of harmonic yields concerning the axes at $45^\circ k$, where $k \in \mathbb{N}$. The odd harmonics are elliptically polarized, when the LP laser deviates from high symmetry axes ($\theta = 45^\circ k$) as shown in Fig. S7(d). It has been explained by Jones matrix formalism in Sec. III C.

VI. CIRCULAR DICHROISM

As shown in Fig. S8(a), we use circularly polarized lights with opposite helicities to excite the TaAs crystal on the x - y and y - z planes respectively. The HHG excited by circular polarized field on the x - z plane is the same as that excited by the field on the y - z plane, because of $\mathcal{C}_{4(z)}$ symmetry. In Figs. S8(b)-(c), we find that the HHG spectra excited by LCP light are identical to those excited by RCP light. Moreover, using Eq. (S11), we obtain the HHG circular dichroism of each order is zero.

VII. ELLIPTICITY DEPENDENCE

In TaAs, we find that the ellipticity dependence of HHG is sensitive to the parameters of driving field. In comparison to the strong laser field in the main text, the laser field with lower intensity and shorter wavelength gives rise to a relatively normal behavior of HHG ellipticity dependence, illustrated in Fig. S9. The yields of 2th, 3th, 6th, 7th, 8th, and 10th harmonics monotonically decay with increasing the driver ellipticity.

Unlike graphene HHG, HHG in TaAs consistently exhibits anomalous behavior, even when the Fermi energy is tuned to be significantly higher ($\varepsilon_F = 1.2$ eV) or lower ($\varepsilon_F = -1.2$ eV) than the energy of the Weyl nodes as shown in Fig. S10.

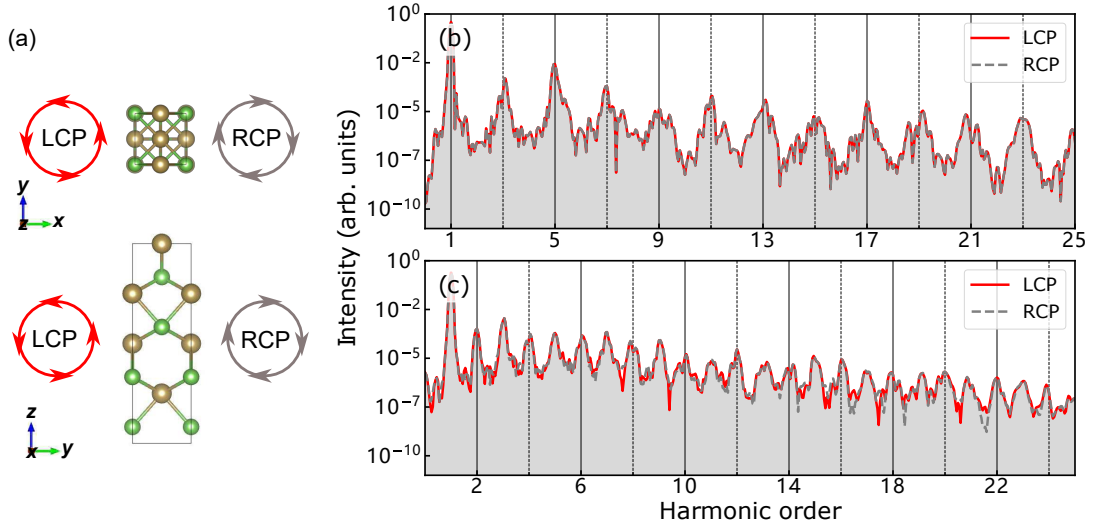


FIG. S8. (a) TaAs lattice driven by LCP and RCP fields in the x - y and y - z planes. HHG spectra excited by LCP and RCP lights, where polarization planes are (b) x - y and (c) y - z , respectively.

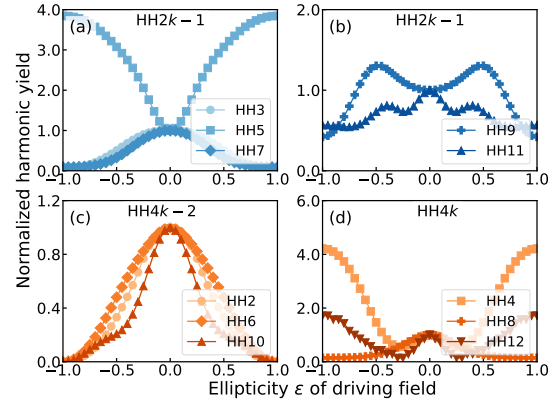


FIG. S9. Ellipticity dependence of HHG in TaAs driven by a weaker laser field. The intensity is $I_0 = 5.6 \times 10^9 \text{ W/cm}^2$ ($E_0 = 0.0004 \text{ a.u.}$), and the wavelength is $\lambda = 3200 \text{ nm}$ ($\hbar\omega = 0.388 \text{ eV}$).

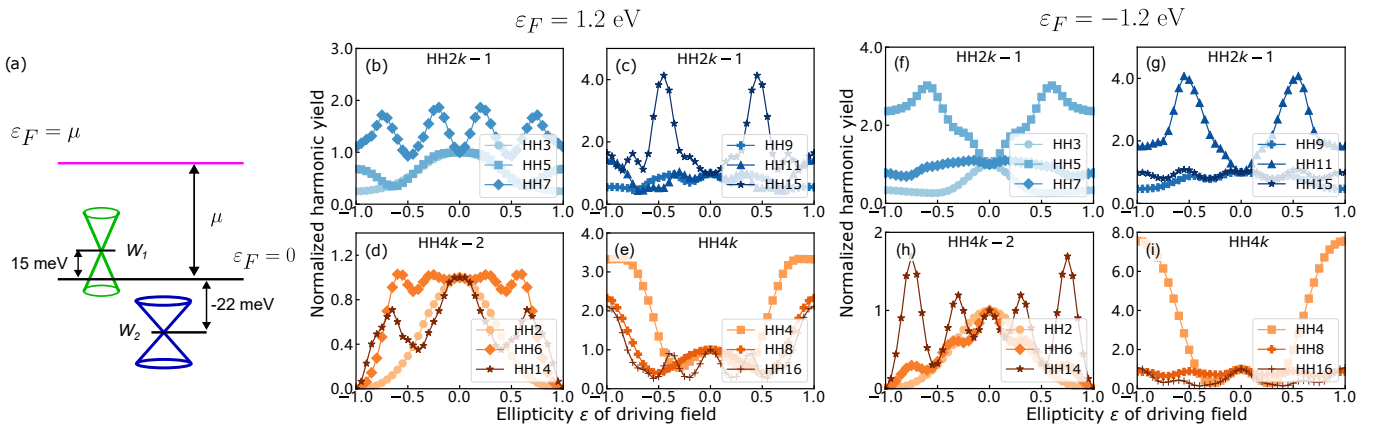


FIG. S10. (a) Relative positions of Weyl cones (W_1 and W_2) and Fermi energy. Fermi energy is shifted by tuning chemical potential μ . Ellipticity dependence of HHG in TaAs with (b)-(e) $\epsilon_F = 1.2 \text{ eV}$ and (f)-(i) $\epsilon_F = -1.2 \text{ eV}$. The laser parameters are the same as those in Fig. S3.

-
- [1] K. Koepernik and H. Eschrig, *Phys. Rev. B* **59**, 1743 (1999).
 - [2] <https://www.fplo.de>.
 - [3] O. Matsyshyn and I. Sodemann, *Phys. Rev. Lett.* **123**, 246602 (2019).
 - [4] K. Koepernik, D. Kasinathan, D. V. Efremov, S. Khim, S. Borisenko, B. Büchner, and J. van den Brink, *Phys. Rev. B* **93**, 201101(R) (2016).
 - [5] Y. Zhang, M. Zhang, W. Yang, H. Yu, M. S. Si, S. Xue, and H. Du, *Phys. Rev. A* **108**, 043508 (2023).
 - [6] R. E. F. Silva, F. Martín, and M. Ivanov, *Phys. Rev. B* **100**, 195201 (2019).
 - [7] G. Fowles, *Introduction to Modern Optics*, 2nd ed. (Dover, 1989).
 - [8] L. Wu, S. Patankar, T. Morimoto, N. L. Nair, E. Thewalt, A. Little, J. G. Analytis, J. E. Moore, and J. Orenstein, *Nat. Phys.* **13**, 350 (2017).